# Doubly charged Higgs production within the Higgs triplet model at future lepton colliders*

Shu-Xiang Li (李书香)[1,2] Ren-You Zhang (张仁友)[1,2,3†] Ming-Hui Liu (刘明辉)[1,2] Xiao-Feng Wang (王晓峰)[1,2]
Zhong-Yuan Liu (刘忠源)[1,2] Yi Jiang (蒋一)[1,2] Liang Han (韩良)[1,2] Qing-hai Wang (王清海)[4‡]

[1]State Key Laboratory of Particle Detection and Electronics, University of Science and Technology of China, Hefei 230026, China
[2]Department of Modern Physics, University of Science and Technology of China, Hefei 230026, China
[3]Anhui Center for Fundamental Sciences in Theoretical Physics, University of Science and Technology of China, Hefei 230026, China
[4]Department of Physics, National University of Singapore, Singapore 117551, Singapore

**Abstract:** We investigate in detail the discovery potential of the doubly charged Higgs boson at the Compact Linear Collider in $e^-e^-$, $e^-\gamma$, $\gamma\gamma$, and $e^+e^-$ collision modes within the Higgs triplet model, using two extreme benchmark points as representatives of the Yukawa-like and gauge-like regions. In the Yukawa-like region, the most promising production mechanism is single production in $e^-e^-$ and $e^-\gamma$ collisions. Given the subsequent decay of the doubly charged Higgs boson into a same-sign lepton pair, CLIC can achieve a statistical significance well beyond the discovery threshold within the parameter space allowed by experimental constraints. In the gauge-like region, using the $\ell^\pm\ell^\pm + \geq 3j$ final state, CLIC exhibits robust discovery potential for the doubly charged Higgs boson up to a mass of approximately 1.2 TeV. We also investigate the search for doubly charged Higgs bosons at the HL-LHC. Our results demonstrate that CLIC offers greater advantages and superior discovery potential for the doubly charged Higgs boson compared with the HL-LHC.

**Keywords:** doubly charged Higgs production, Higgs triplet model, lepton colliders

**DOI:** 10.1088/1674-1137/ae9f38 **CSTR:** 32044.14.ChinesePhysicsC.50

CPC Accepted

## I. INTRODUCTION

The discovery of neutrino oscillations [1−3] marks a pivotal milestone in particle physics, providing compelling experimental evidence that neutrinos have nonzero masses. Cosmological data tightly constrain the sum of neutrino masses [4], while tritium $\beta$-decay experiments provide direct, albeit presently less sensitive, upper limits on the effective electron antineutrino mass [5]. Taken together, these observations point to a neutrino mass scale in the sub-eV range, possibly below $O(10^{-1}\,\text{eV})$. However, the Standard Model (SM) cannot naturally account for nonzero neutrino masses. Even when right-handed neutrinos are incorporated into the SM, generating neutrino masses consistent with experimental constraints solely through Dirac mass terms requires an extraordinarily small Yukawa coupling, $Y_\nu \lesssim 10^{-12}$, thereby posing a severe naturalness problem. This tension is effectively resolved within the seesaw framework, in which heavy Majorana neutrinos generate light neutrino masses via the dimension-five operator LLHH/$\Lambda$ [6], thereby explaining the observed neutrino mass scale without assuming an unnaturally small Yukawa coupling. The seesaw mechanism [7−9] can be classified into three distinct types according to the gauge representations of the heavy fields introduced to generate the dimension-five Weinberg operator [10]: Type-I, introducing right-handed fermion singlets [11]; Type-II, involving left-handed scalar triplets [12−14]; and Type-III, incorporating fermion triplets [15].

The Higgs triplet model (HTM) [16−18] provides a minimal realization of the Type-II seesaw mechanism by extending the SM scalar sector with an $SU(2)_L$ triplet. After electroweak symmetry breaking (EWSB), the Higgs triplet $\Delta$ acquires a vacuum expectation value (VEV) $v_\Delta$, inducing Majorana masses for the neutrinos through its Yukawa couplings to the left-handed lepton doublets, $m_\nu = \sqrt{2}v_\Delta Y$. The mixing between the scalar triplet and the SM Higgs doublet yields five physical scalar states.

Received 7 August 2026; Accepted 25 August 2026; Accepted manuscript online 26 August 2026
* Supported by the National Natural Science Foundation of China (2061141005) and the CAS Center for Excellence in Particle Physics (CCEPP)
† E-mail: zhangry@ustc.edu.cn
‡ E-mail: qhwang@nus.edu.sg
Content from this work may be used under the terms of the Creative Commons Attribution 3.0 licence. Any further distribution of this work must maintain attribution to the author(s) and the title of the work, journal citation and DOI. Article funded by SCOAP[3] and published under licence by Chinese Physical Society and the Institute of High Energy Physics of the Chinese Academy of Sciences and the Institute of Modern Physics of the Chinese Academy of Sciences and IOP Publishing Ltd

Among these, the doubly charged Higgs boson $H^{\pm\pm}$ exhibits distinctive collider signatures because of its unique electric charge and characteristic decay modes. Consequently, $H^{\pm\pm}$ has been a central focus of HTM phenomenology studies [19−27], with particular emphasis on its production at current and future hadron colliders, including the Large Hadron Collider (LHC), the High-Luminosity LHC (HL-LHC) [28], and the Future Circular Collider (FCC) [29]. The dominant mechanisms for $H^{\pm\pm}$ production are Drell–Yan pair production, associated production with a singly charged Higgs boson, and vector-boson fusion. At the LHC, the pair-production cross section of $H^{\pm\pm}$ ranges from approximately $10^3$ fb to $10^{-3}$ fb as its mass increases from 100 GeV to 1.8 TeV [30]. The decay channels of $H^{\pm\pm}$ have also been systematically investigated [31], with the dominant modes being $H^{\pm\pm}\to\ell^\pm\ell^\pm$, $H^{\pm\pm}\to W^\pm W^\pm$, and $H^{\pm\pm}\to H^\pm f\bar{f}'$ when $m_{H^{\pm\pm}}>m_{H^\pm}$ for the normal mass hierarchy of the triplet-like scalars.

In addition to $pp$ collisions, other collision modes have also been studied in the literature, including $e^-p$ [32], $e^+e^-$ [33−36], $e^-e^-$ [37], $e^-\gamma$ [38, 39], and $\gamma\gamma$ [40, 41]. The production of $H^{\pm\pm}$ at $\mu^+\mu^-$ colliders has also been investigated within the Type-II seesaw framework [42−44]. These analyses collectively covered $H^{++}H^{--}$ pair production, $H^{\pm\pm}H^{\mp}$ associated production, and $H^{\pm\pm}$ single production, examined both leptonic and bosonic decay modes, and quantified the sensitivity of future muon colliders to $H^{\pm\pm}$ with masses in the TeV and multi-TeV ranges. Most of the aforementioned lepton-based collision modes operate at lower center-of-mass energies than $pp$ collisions, which limits the accessible parameter space for $m_{H^{\pm\pm}}$. The ATLAS experiment, assuming $Br(H^{\pm\pm}\to\ell^\pm\ell^\pm)=1/6$ $(\ell=e,\mu,\tau)$, sets a lower bound of 1080 GeV on $m_{H^{\pm\pm}}$, which exceeds the kinematic reach of current lepton colliders. The Compact Linear Collider (CLIC), proposed to operate at $\sqrt{s}=1.5$ TeV in stage II and $\sqrt{s}=3.0$ TeV in stage III [45], provides opportunities for probing TeV-scale $H^{\pm\pm}$. Moreover, lepton colliders feature much cleaner backgrounds; therefore, the prospects for discovering $H^{\pm\pm}$ at high-energy lepton colliders may be superior to those at hadron colliders.

In this paper, we systematically investigate the discovery potential of $H^{\pm\pm}$ at CLIC within the HTM in $e^-e^-$, $e^-\gamma$, $\gamma\gamma$, and $e^+e^-$ collisions, focusing on two representative regions of parameter space: the Yukawa-like and gauge-like regions. It should be noted that the $e^-e^-$ collision mode is not included in the baseline CLIC running program, but was discussed as a possible collision option in early CLIC studies [46, 47]. Moreover, this collision option has also been considered in phenomenological studies at the CLIC design energy of 3 TeV [48, 49]. In the HTM, the $e^-e^-$ mode is particularly well suited to searches for $H^{--}$ in the Yukawa-like region, since the single production of $H^{--}$ in this mode proceeds directly through the triplet Yukawa coupling to electrons. We therefore include this mode in our CLIC analysis as a benchmark scenario. For comparison, we also assess the discovery prospects at the HL-LHC via pair production of the doubly charged Higgs boson. The rest of this paper is organized as follows. In Section II, we briefly review the HTM and summarize the theoretical and experimental constraints on the model parameters. Section III discusses the dominant production channels of the doubly charged Higgs boson at both CLIC and the LHC. In Section IV, we analyze the discovery prospects of the doubly charged Higgs at CLIC, while Section V presents the corresponding analysis at the HL-LHC for comparison. Finally, a concise summary of our findings is given in Section VI.

## II. HIGGS TRIPLET MODEL

The Higgs triplet model extends the particle content of the standard model by introducing a complex $SU(2)_L$ triplet scalar field with hypercharge $Y=2$. The scalar triplet $\Delta$ and the SM Higgs doublet $\Phi$ are commonly parameterized as follows:

$$\Delta=\frac{1}{\sqrt{2}}\begin{pmatrix}\delta^+ & \sqrt{2}\delta^{++}\\ \delta^0+\mathrm{i}\xi^0+v_\Delta & -\delta^+\end{pmatrix},$$
$$\Phi=\frac{1}{\sqrt{2}}\begin{pmatrix}\sqrt{2}\phi^+\\ \phi^0+\mathrm{i}\eta^0+v_\Phi\end{pmatrix}, \tag{1}$$

where $v_\Delta$ and $v_\Phi$ denote the vacuum expectation values of the neutral components of $\Delta$ and $\Phi$, respectively.

The Higgs sector of the HTM is governed by the following Lagrangian:

$$\mathcal{L}_{\rm HTM}=(D^\mu\Phi)^\dagger\left(D_\mu\Phi\right)+\mathrm{Tr}\left[(D^\mu\Delta)^\dagger\left(D_\mu\Delta\right)\right]+\mathcal{L}_{\rm Yukawa}-V(\Phi,\Delta). \tag{2}$$

The covariant derivatives of $\Phi$ and $\Delta$ appearing in the kinetic terms are given by

$$D_\mu\Phi=\partial_\mu\Phi+\mathrm{i}\frac{g_1}{2}V_{1\mu}\Phi+\mathrm{i}\frac{g_2}{2}V_{2\mu}^i\tau^i\Phi,$$
$$D_\mu\Delta=\partial_\mu\Delta+\mathrm{i}g_1V_{1\mu}\Delta+\mathrm{i}\frac{g_2}{2}V_{2\mu}^i\left[\tau_i,\Delta\right], \tag{3}$$

where $V_{1\mu}$ and $V_{2\mu}^i$ $(i=1,2,3)$ denote the $U(1)_Y$ and $SU(2)_L$ gauge fields, respectively; $g_1$ and $g_2$ are the corresponding coupling constants; and $\tau^i$ are the Pauli matrices. The Yukawa terms for the Type-II seesaw mechanism are

$$\mathcal{L}_{\rm Yukawa}\supset\mathcal{L}_{\rm seesaw}=-Y_{ij}\overline{L_i^c}\,\mathrm{i}\tau^2\Delta L_j+\mathrm{h.c.}, \tag{4}$$

CPC Accepted

where $L_i = (\nu_i, \ell_i)^T$ are the left-handed lepton doublets, the superscript $c$ denotes Dirac charge conjugation, and $Y$ is the Yukawa coupling matrix. After electroweak symmetry breaking, the left-handed neutrino states $\nu_i$ acquire Majorana masses

$$m_\nu = \sqrt{2} v_\Delta Y, \tag{5}$$

which is diagonalized by the Pontecorvo–Maki–Nakagawa–Sakata (PMNS) mixing matrix $U$ as

$$m_\nu = U^* \mathrm{diag}(m_1, m_2, m_3) U^\dagger, \tag{6}$$

where $m_1$, $m_2$, and $m_3$ are the masses of the three neutrino mass eigenstates. A detailed discussion of $m_\nu$ and $Y$ will be provided in Sec. II.B.

### A. Scalar potential and Higgs mass spectrum

The general HTM scalar potential can be written as

$$\begin{aligned} V(\Phi, \Delta) = & -\mu_\Phi^2 \Phi^\dagger\Phi - \mu_\Delta^2 \mathrm{Tr}\left(\Delta^\dagger\Delta\right) + \frac{\lambda}{4}\left(\Phi^\dagger\Phi\right)^2 \\ & + \lambda_1 \Phi^\dagger\Phi \,\mathrm{Tr}\left(\Delta^\dagger\Delta\right) + \lambda_2 \left[\mathrm{Tr}\left(\Delta^\dagger\Delta\right)\right]^2 \\ & + \lambda_3 \mathrm{Tr}\left(\Delta^\dagger\Delta\Delta^\dagger\Delta\right) + \lambda_4 \Phi^\dagger\Delta\Delta^\dagger\Phi \\ & + \mu\left(\Phi^T \mathrm{i}\tau^2 \Delta^\dagger \Phi + \mathrm{h.c.}\right), \end{aligned} \tag{7}$$

where $\mu_\Phi$ and $\mu_\Delta$ are mass parameters, and $\lambda$ and $\lambda_{1-4}$ are quartic scalar coupling constants. Using the identity

$$\Phi^\dagger\Delta\Delta^\dagger\Phi + \Phi^\dagger\Delta^\dagger\Delta\Phi = \Phi^\dagger\Phi \,\mathrm{Tr}\left(\Delta^\dagger\Delta\right), \tag{8}$$

the operator $\Phi^\dagger\Delta^\dagger\Delta\Phi$ can be expressed in terms of other structures and is therefore redundant in the HTM potential. The parameter $\mu$ in the scalar potential has mass dimension one and explicitly breaks the global $U(1)$ lepton number symmetry. Although $\mu$ is generally complex, it can be rendered real by an appropriate phase rotation of the field combination $\Phi^T \mathrm{i}\tau^2 \Delta^\dagger \Phi$ [18, 50].

After EWSB, the minimization conditions of the Higgs potential imply that the mass parameters can be determined by the Higgs VEVs, the quartic scalar couplings, and the lepton-number-violating trilinear scalar coupling as follows:

$$\begin{aligned} \mu_\Phi^2 &= \frac{1}{4}\lambda v_\Phi^2 + \frac{1}{2}\lambda_{14} v_\Delta^2 - \sqrt{2}\mu v_\Delta, \\ \mu_\Delta^2 &= \frac{1}{2}\lambda_{14} v_\Phi^2 + \lambda_{23} v_\Delta^2 - \frac{\mu v_\Phi^2}{\sqrt{2} v_\Delta}, \end{aligned} \tag{9}$$

where $\lambda_{ab} \equiv \lambda_a + \lambda_b$ $(a, b = 1, 2, 3, 4)$. The Higgs mass eigenstates in the HTM arise from mixing among the field components given in Eq. (1). The doubly charged scalar fields $\delta^{\pm\pm}$ are already mass eigenstates and are therefore also denoted by $H^{\pm\pm}$. The fields $\delta^\pm$ and $\phi^\pm$ mix to form the singly charged Higgs bosons $H^\pm$ and the Goldstone bosons $G^\pm$, which provide the longitudinal degrees of freedom of the $W^\pm$ bosons. Similarly, the mixing of the two $\mathcal{CP}$-odd neutral fields, $\xi^0$ and $\eta^0$, gives rise to the pseudoscalar $A^0$ and the Goldstone boson $G^0$, which is absorbed by the $Z^0$ boson. Diagonalizing the mass matrix of the $\mathcal{CP}$-even neutral Higgs sector, spanned by $\delta^0$ and $\phi^0$, yields two massive scalar states, $H^0$ and $h^0$. The lighter mass eigenstate, $h^0$, is identified as the 125 GeV Higgs boson observed experimentally. The rotation angles (also referred to as mixing angles) $\beta_\pm$, $\beta_0$, and $\alpha$, corresponding respectively to the transformations from the gauge basis to the mass basis for the singly charged, $\mathcal{CP}$-odd neutral, and $\mathcal{CP}$-even neutral Higgs sectors, are given by

$$\begin{aligned} \tan\beta_\pm &= \frac{1}{\sqrt{2}}\tan\beta_0 = \frac{\sqrt{2} v_\Delta}{v_\Phi}, \\ \tan\alpha &= -\frac{\sqrt{(A-C)^2 + 4B^2} + (A-C)}{2B}, \end{aligned} \tag{10}$$

where

$$A = \frac{1}{2}\lambda v_\Phi^2, \quad B = \lambda_{14} v_\Phi v_\Delta - 2 m_\Delta^2 \frac{v_\Delta}{v_\Phi}, \quad C = m_\Delta^2 + 2\lambda_{23} v_\Delta^2, \tag{11}$$

where $m_\Delta$ denotes an intermediate mass parameter related to $\mu$ through $m_\Delta^2 = \mu v_\Phi^2 / \sqrt{2} v_\Delta$. Accordingly, the scalar mass spectrum of the HTM can be expressed in terms of the parameters $\{v_\Phi, v_\Delta, m_\Delta, \lambda, \lambda_{1-4}\}$ as follows:

$$\begin{aligned} & m_{H^{\pm\pm}}^2 = m_\Delta^2 - \lambda_3 v_\Delta^2 - \frac{\lambda_4}{2} v_\Phi^2, \quad m_{A^0}^2 = m_\Delta^2\left(1 + \frac{4 v_\Delta^2}{v_\Phi^2}\right), \\ & m_{H^\pm}^2 = \left(m_\Delta^2 - \frac{\lambda_4}{4} v_\Phi^2\right)\left(1 + \frac{2 v_\Delta^2}{v_\Phi^2}\right), \\ & m_{h^0, H^0}^2 = \frac{1}{2}\left[(A + C) \mp \sqrt{(A-C)^2 + 4B^2}\right]. \end{aligned} \tag{12}$$

### B. Constraints on HTM parameters

#### 1. *Theoretical constraints on Higgs quartic couplings*

In the Higgs potential of the HTM, the quartic coupling constants ($\lambda$ and $\lambda_{1,2,3,4}$) are subject to three theoretical constraints: perturbativity, vacuum stability, and perturbative unitarity. Specifically, perturbativity requires all couplings to remain within the perturbative regime [51, 52]; vacuum stability requires the Higgs potential to be bounded from below in all directions in field space [18, 53−55]; and perturbative unitarity constrains scattering

CPC Accepted

amplitudes to remain finite at high energies [18, 52, 55].

• Perturbativity:

$$|\lambda| < 4\pi, \quad |\lambda_a| < 4\pi \quad (a = 1, 2, 3, 4). \tag{13}$$

• Vacuum stability:

$$\begin{aligned}
&\lambda > 0, \quad \lambda_2 + \lambda_3 > 0, \quad 2\lambda_2 + \lambda_3 > 0, \\
&\lambda_1 + \sqrt{\lambda(\lambda_2 + \lambda_3)} > 0, \quad \lambda_1 + \lambda_4 + \sqrt{\lambda(\lambda_2 + \lambda_3)} > 0, \\
&\max\Big\{ |\lambda_4| \sqrt{\lambda_2 + \lambda_3} - \lambda_3 \sqrt{\lambda}, 2\lambda_1 + \lambda_4 \\
&+ \sqrt{(2\lambda - \lambda_4^2/\lambda_3)(2\lambda_2 + \lambda_3)} \Big\} > 0.
\end{aligned} \tag{14}$$

• Perturbative unitarity:[1)]

$$\begin{aligned}
&|\lambda| < 2\kappa\pi, \quad |\lambda_1| < \kappa\pi, \quad 2|\lambda_2| < \kappa\pi, \quad |\lambda_1 + \lambda_4| < \kappa\pi, \\
&|2\lambda_1 - \lambda_4| < 2\kappa\pi, \quad |2\lambda_1 + 3\lambda_4| < 2\kappa\pi, \quad 2|\lambda_2 + \lambda_3| < \kappa\pi, \\
&|2\lambda_2 - \lambda_3| < \kappa\pi, \\
&\left|\lambda + 4\lambda_2 + 8\lambda_3 \pm \sqrt{(\lambda - 4\lambda_2 - 8\lambda_3)^2 + 16\lambda_4^2}\right| < 4\kappa\pi, \\
&\left|3\lambda + 16\lambda_2 + 12\lambda_3 \pm \sqrt{(3\lambda - 16\lambda_2 - 12\lambda_3)^2 + 24(2\lambda_1 + \lambda_4)^2}\right| \\
&< 4\kappa\pi.
\end{aligned} \tag{15}$$

### 2. *Experimental constraints on $v_\Delta$, Higgs masses and Yukawa couplings*

In the HTM, the masses of the $W^\pm$ and $Z^0$ bosons, which arise from the kinetic terms of the Higgs multiplets in Eq.(2), are given by

$$m_{W^\pm} = \frac{g_2}{2}\sqrt{v_\Phi^2 + 2v_\Delta^2}, \quad m_{Z^0} = \frac{g_2}{2\cos\theta_W}\sqrt{v_\Phi^2 + 4v_\Delta^2}, \tag{16}$$

where the Weinberg angle $\theta_W$ is defined by $\cos\theta_W = g_2/\sqrt{g_1^2 + g_2^2}$. The corresponding $\rho$ parameter is then given by

$$\rho \equiv \frac{m_{W^\pm}^2}{m_{Z^0}^2 \cos^2\theta_W} = \frac{1 + 2v_\Delta^2/v_\Phi^2}{1 + 4v_\Delta^2/v_\Phi^2}. \tag{17}$$

In contrast to the tree-level prediction $\rho = 1$ in the SM, the HTM predicts $\rho < 1$. Electroweak precision measurements give $\rho = 1.0001 \pm 0.0009$ at the $1\sigma$ confidence level (CL) [56], implying $v_\Delta^2/v_\Phi^2 < 4 \times 10^{-4}$. Combined with the relation $\sqrt{v_\Phi^2 + 2v_\Delta^2} \simeq 246$ GeV, this result leads to an upper bound of $v_\Delta < 4.9$ GeV on the VEV of the Higgs triplet. In the limit $v_\Delta \ll v_\Phi$, the scalar spectrum of the HTM can be approximated at leading order as

$$\begin{aligned}
&m_{h^0}^2 = \frac{\lambda}{2}v_\Phi^2, && m_{H^\pm}^2 = m_\Delta^2 - \frac{\lambda_4}{4}v_\Phi^2, \\
&m_{A^0}^2 = m_{H^0}^2 = m_\Delta^2, && m_{H^{\pm\pm}}^2 = m_\Delta^2 - \frac{\lambda_4}{2}v_\Phi^2.
\end{aligned} \tag{18}$$

The mass of $h^0$ is determined solely by the Higgs doublet quartic self-coupling $\lambda$ and its VEV $v_\Phi$, as in the SM. By contrast, the masses of the other exotic Higgs bosons are set by the characteristic mass scale $m_\Delta$ of the HTM, with their mass splittings governed by $\lambda_4$. For $\lambda_4 < 0$, the scalar spectrum exhibits a normal mass hierarchy (NMH), $m_{H^{\pm\pm}} > m_{H^\pm} > m_{A^0,H^0}$, whereas for $\lambda_4 > 0$, it follows an inverted mass hierarchy (IMH), $m_{H^{\pm\pm}} < m_{H^\pm} < m_{A^0,H^0}$.

The existence of a doubly charged Higgs boson is a hallmark prediction of many extensions of the SM, including the Type-II seesaw model, left-right symmetric models, and various radiative neutrino-mass models (e.g., the Zee–Babu model). In proton-proton collisions at the LHC, searches for doubly charged Higgs bosons have primarily focused on Drell–Yan pair and associated production, $q\bar{q} \to Z^0/\gamma \to H^{\pm\pm}H^{\mp\mp}$ and $q\bar{q}' \to W^\pm \to H^{\pm\pm}H^\mp$, with subsequent fermionic or bosonic decays—manifesting as same-sign dileptons or $W^\pm W^\pm$ pairs, respectively—determined by the triplet VEV and Yukawa couplings. During Run 2 of the LHC, both ATLAS and CMS analyzed events with same-sign lepton pairs in two-, three-, and four-lepton final states to search for doubly charged Higgs bosons, which provide relatively clean experimental signatures with low SM backgrounds [57−60]. No significant excess over the SM predictions was observed; consequently, these searches have set lower limits on the mass of the doubly charged Higgs boson, as summarized in Table 1. It is important to emphasize that these mass limits depend strongly on several assumptions, including the production mode, chirality, and decay branching fractions. For $H^{\pm\pm}$ decaying predominantly into same-sign light leptons and produced in pairs, the most stringent direct limit from LHC Run 2—established by the ATLAS measurement using the full 139 fb$^{-1}$ dataset—is approximately 1.08 TeV. By contrast, for the bosonic decay channel $H^{\pm\pm} \to W^\pm W^\pm$, current mass exclusion limits reach only a few hundred GeV—350 GeV for pair production and 230 GeV for associated production—because of more challenging backgrounds.

As shown in Eq. (18), the mass spectrum of the triplet-like scalar states in the HTM is determined by $m_\Delta$ and $\lambda_4$. Accordingly, the limits from direct searches for $H^{\pm\pm}$, $H^\pm$, and $H^0/A^0$, together with constraints on the scalar mass splitting from electroweak precision measurements, can be recast as constraints on the $(m_\Delta, \lambda_4)$ para-

1) In this work, the parameter $\kappa$ is fixed at 8.

CPC Accepted

**Table 1.** Observed 95% CL lower limits on the $H^{\pm\pm}$ mass from analyses of LHC Run 2 data. In the CMS search using the 12.9 fb$^{-1}$ dataset, the benchmark points BP1–BP4 correspond to four distinct branching-fraction scenarios for $H^{\pm\pm}$ decays, each associated with a different neutrino mass hierarchy.

| Experiment | Data sample | Benchmark | Observed lower limit [GeV] | | |
|---|---|---|---|---|---|
| ATLAS | 36.1 fb$^{-1}$ [57] | Pair production | $H_L^{\pm\pm}$ | $H_R^{\pm\pm}$ | |
| | | $\mathrm{Br}(H^{\pm\pm}\to e^\pm e^\pm)=100\%$ | 768 | 658 | |
| | | $\mathrm{Br}(H^{\pm\pm}\to e^\pm \mu^\pm)=100\%$ | 875 | 761 | |
| | | $\mathrm{Br}(H^{\pm\pm}\to \mu^\pm \mu^\pm)=100\%$ | 846 | 723 | |
| | | $\sum_{\ell,\ell'=e,\mu}\mathrm{Br}(H^{\pm\pm}\to \ell^\pm\ell'^\pm)=10\%$ | 450 | 320 | |
| | 139 fb$^{-1}$ [58, 59] | Pair production | LR model | –Zee–Babu model | |
| | | $\mathrm{Br}(H^{\pm\pm}\to \ell^\pm\ell'^\pm)=1/6,\ (\ell,\ell'=e,\mu,\tau)$ | 1080 | 900 | |
| | | Pair and associated production | Pair Prod. | Assoc. Prod. | |
| | | $\mathrm{Br}(H^{\pm\pm}\to W^\pm W^\pm)=100\%$ | 350 | 230 | |
| CMS | 12.9 fb$^{-1}$ [60] | Pair and associated production | Pair Prod. | Assoc. Prod. | Combined |
| | | $\mathrm{Br}(H^{\pm\pm}\to e^\pm e^\pm)=100\%$ | 652 | 734 | 800 |
| | | $\mathrm{Br}(H^{\pm\pm}\to e^\pm \mu^\pm)=100\%$ | 665 | 750 | 820 |
| | | $\mathrm{Br}(H^{\pm\pm}\to \mu^\pm \mu^\pm)=100\%$ | 712 | 746 | 816 |
| | | $\mathrm{Br}(H^{\pm\pm}\to e^\pm \tau^\pm)=100\%$ | 481 | 568 | 714 |
| | | $\mathrm{Br}(H^{\pm\pm}\to \mu^\pm \tau^\pm)=100\%$ | 537 | 518 | 643 |
| | | $\mathrm{Br}(H^{\pm\pm}\to \tau^\pm \tau^\pm)=100\%$ | 396 | 479 | 535 |
| | | BP1 | 519 | 613 | 723 |
| | | BP2 | 465 | 670 | 716 |
| | | BP3 | 531 | 706 | 761 |
| | | BP4 | 496 | 639 | 722 |

CPC Accepted

meter space. The mass limits on $H^{\pm\pm}$ from direct searches are summarized in Table 1. For the singly charged Higgs boson, the ATLAS Collaboration performed a search in multilepton final states via $H^{\pm\pm}H^{\mp}$ associated production, excluding masses up to about 230 GeV for $m_{H^{\pm\pm}}\simeq m_{H^\pm}$ [59]. Vector-boson-fusion production of $H^\pm$, followed by the decay $H^\pm\to W^\pm Z$, was also investigated by ATLAS and CMS, yielding upper limits on $\sigma_{\mathrm{VBF}}(H^\pm)\times\mathrm{Br}(H^\pm\to W^\pm Z)$ [61, 62]. For heavy neutral Higgs bosons, both experiments conducted searches in the $\tau^+\tau^-$ final state through gluon-gluon fusion and $b$-associated production, setting upper limits on the corresponding $\sigma\times\mathrm{Br}$ [63, 64]. These direct searches generally constrain the $(m_\Delta,\lambda_4)$ parameter space. Electroweak precision measurements, in turn, restrict the mass splitting $\Delta m\equiv m_{H^{\pm\pm}}-m_{H^\pm}$, with the allowed range summarized as [53, 55]

$$-50\ \mathrm{GeV}\lesssim\Delta m\lesssim 40\ \mathrm{GeV}\,. \tag{19}$$

From Eq. (18), the mass splitting is given by

$$\Delta m=-\frac{\lambda_4 v_\Phi^2}{4\,(m_{H^{\pm\pm}}+m_{H^\pm})}\,, \tag{20}$$

and for $m_{H^{\pm\pm}}\simeq m_{H^\pm}\simeq m_\Delta$, this relation simplifies to $\Delta m\simeq-\lambda_4 v_\Phi^2/(8m_\Delta)$. Thus, for fixed $\lambda_4$, electroweak precision measurements and direct searches for triplet-like Higgs bosons together impose a constraint on $m_\Delta$.

In the HTM, neutrino masses arise from Yukawa interactions between the scalar triplet and the left-handed lepton doublets, and experimental measurements of these masses directly constrain the Yukawa coupling matrix. Based on 259 days of data, the KArlsruhe TRItium Neutrino (KATRIN) experiment has set the most recent direct limit on the effective electron antineutrino mass, $m_\nu<0.45$ eV, at 90% CL [5]. In addition, the Planck Collaboration, in combination with baryon acoustic oscillation (BAO) measurements, has established an upper limit on the sum of neutrino masses, $\sum m_\nu<0.12$ eV, at 95% CL [4]. These complementary constraints provide stringent bounds on the neutrino mass scale from both laboratory experiments and cosmological observations. A more direct and stringent set of constraints on the Yukawa coup-

ling matrix is obtained from measurements of the branching ratios of lepton-flavor-violating processes [65−67], the anomalous magnetic moments of the electron [68] and muon [69], the muonium-antimuonium oscillation probability [70], and the Bhabha-scattering cross sections [71], all of which have been comprehensively reviewed in the literature [57, 72]. In particular, the measurement of Bhabha scattering imposes a direct constraint on the diagonal element $Y_{ee}$, yielding $|Y_{ee}|^2 < 0.12\times(m_{H^{\pm\pm}}/1\,\mathrm{TeV})^2$. By contrast, constraints from other observables typically involve bilinear combinations of diagonal and off-diagonal Yukawa couplings, implying that sizable diagonal entries must be accompanied by sufficiently small off-diagonal ones. Such a Yukawa texture, however, poses a significant challenge for reproducing the observed PMNS mixing, reflecting the inherent tension between accommodating large diagonal couplings and maintaining the observed neutrino flavor structure. A viable solution is the hybrid seesaw mechanism, which incorporates both Type-II and Type-I contributions [13], with neutrino dynamics governed by

$$\mathcal{L}_{\text{seesaw}}^{\text{hybrid}} = -Y_{ij}\overline{L_i^c}\,\mathrm{i}\tau^2\Delta L_j - g_{ij}\overline{L}_i\widetilde{\Phi}N_j - \frac{1}{2}M_{ij}\overline{N_i^c}N_j + \text{h.c.}, \quad (21)$$

where $N_i$ denote the right-handed neutrino singlets. In this hybrid seesaw framework, the Type-I sector determines the off-diagonal structure of the neutrino mass matrix, while the Type-II contribution primarily sets the diagonal entries. This yields a mass-matrix texture that naturally reproduces the observed neutrino mixing pattern and remains compatible with a sizable $Y_{ee}$. In our calculation, we adopt the single-flavor-dominance hypothesis, retaining only the $Y_{ee}$ coupling, which is allowed to approach its experimental upper limit.

### C. HTM input parameters

After EWSB, the Higgs potential in the HTM is fully specified by eight parameters, $\{v_\Phi, v_\Delta, m_\Delta, \lambda, \lambda_{1-4}\}$, of which only seven are independent because of the electroweak constraint $\sqrt{v_\Phi^2+2v_\Delta^2}\simeq 246\,\mathrm{GeV}$. In phenomenological studies, however, it is often more convenient to use physical observables, such as particle masses or mixing angles, as input parameters. In this work, focusing on the phenomenology of the doubly charged Higgs boson, we adopt $m_{H^{\pm\pm}}$ as one of the fundamental input parameters, while the mass of the lighter $\mathcal{CP}$-even scalar, $m_{h^0}$, is fixed at 125 GeV, corresponding to the experimentally observed Higgs boson. For simplicity, the remaining five independent input parameters of the Higgs potential are chosen to be $v_\Delta$ and $\lambda_{1-4}$, without referring to the masses of the other Higgs states. Notably, this input scheme effectively avoids a potential fine-tuning problem. As shown in Eq.(18), the neutral scalars $A^0$ and $H^0$ are degenerate in mass in the small-$v_\Delta$ regime, as required by the $\rho$-parameter constraint. Treating both $m_{A^0}$ and $m_{H^0}$ as input parameters would inevitably require fine-tuning these masses to preserve the perturbativity of the Higgs potential [22].

In the Yukawa sector, because the production cross section of the doubly charged Higgs boson at lepton colliders is insensitive to the non-$ee$ elements of the Yukawa coupling matrix, we adopt the single-flavor-dominance hypothesis, setting $Y_{ij} = Y_{ee}\delta_{ie}\delta_{je}$. This hypothesis defines a benchmark scenario for the flavor structure of the triplet Yukawa coupling matrix. Thus, together with the Higgs potential parameters introduced above, the HTM is fully specified by the following seven independent parameters,

$$\{m_{H^{\pm\pm}}, v_\Delta, \lambda_{1-4}, Y_{ee}\}, \quad (22)$$

with values yet to be determined. A detailed description of the input scheme for these parameters is given below.

• $\lambda_{1-4}$:

The production and decay channels of the doubly charged Higgs boson studied in this work are independent of the quartic scalar couplings $\lambda_1$ and $\lambda_2$. The dependence on $\lambda_3$ arises exclusively through the $H^{\pm\pm}H^{\mp}H^{\mp}$ Higgs self-coupling. Owing to the strong suppression by the small $v_\Delta$, this dependence can be safely neglected. Therefore, $\lambda_3$ is set to zero throughout the analysis for simplicity. As shown in Eq. (18), $\lambda_4$ fully determines the mass hierarchy of the Higgs spectrum. In the NMH scenario considered here, we take $\lambda_4 = -2$ as a representative value that is consistent with both theoretical and experimental constraints and reflects a typical mass-splitting pattern.

• $Y_{ee}$, $v_\Delta$ and $m_{H^{\pm\pm}}$:

The decay pattern of the doubly charged Higgs boson is primarily determined by its mass, the mass splitting between the doubly and singly charged Higgs states, and the relative strengths of the Yukawa and gauge couplings of the Higgs triplet. Figure 1 illustrates the branching ratios of the dominant decay channels of the doubly charged Higgs boson as functions of $v_\Delta$ for various Higgs masses, assuming $\sqrt{2}v_\Delta Y_{ee} = 0.1$ eV. As $m_{H^{\pm\pm}}$ increases from 400 GeV to 2500 GeV, the mass splitting $\Delta m$ gradually decreases from approximately 40 GeV to about 6 GeV. In the small-$v_\Delta$ regime, decays of the doubly charged Higgs are dominated by Yukawa interactions and proceed primarily into same-sign dilepton final states. As $v_\Delta$ increases, three-body decays into a singly charged Higgs boson and a pair of light fermions become increasingly significant. At sufficiently large $v_\Delta$, the decays are governed by gauge interactions, making the same-sign $W$-pair channel the dominant mode. Although the NMH

CPC Accepted

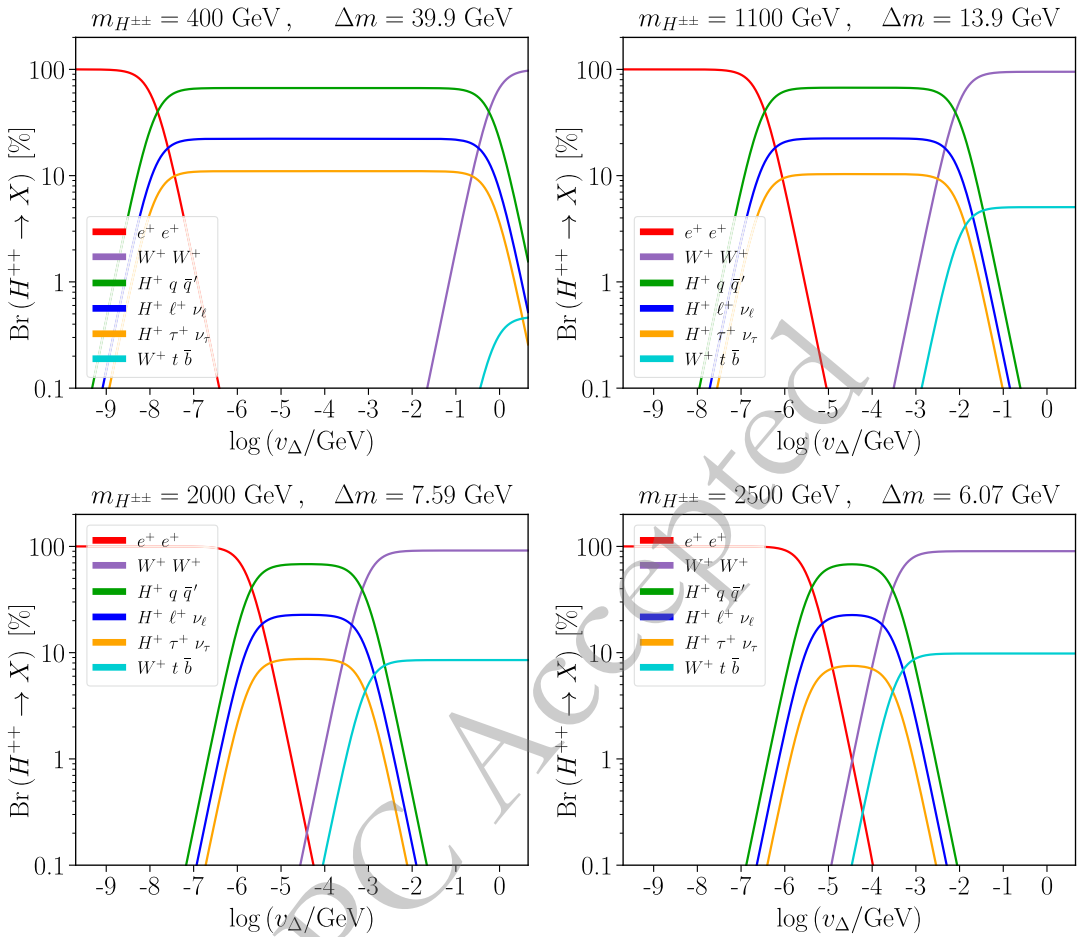



**Fig. 1.** (color online) Branching ratios of the dominant decay channels of $H^{++}$ as functions of $v_\Delta$ for different Higgs masses, with $\sqrt{2}v_\Delta Y_{ee} = 0.1$ eV.

CPC Accepted

scenario permits decays into singly charged Higgs bosons, we confine our analysis to the Yukawa-like and gauge-like regions and explicitly exclude the intermediate-$v_\Delta$ regime. In these two limits, $H^{\pm\pm}$ decays almost exclusively into $e^\pm e^\pm$ and $W^\pm W^\pm$, with $\text{Br}(H^{\pm\pm} \to e^\pm e^\pm) \simeq 100\%$ and $\text{Br}(H^{\pm\pm} \to W^\pm W^\pm) \simeq 100\%$, respectively. Unless otherwise specified, the subsequent analysis is performed at the following two extreme benchmark points in the $(v_\Delta, Y_{ee})$ parameter space:

$$\begin{aligned} \text{BP1}: \quad & (v_\Delta = 2\times10^{-10}\ \text{GeV}, \quad Y_{ee} = 0.35) \\ & \in \ \text{Yukawa-like region}, \\ \text{BP2}: \quad & (v_\Delta = 4.5\ \text{GeV}, \quad Y_{ee} = 1.5\times10^{-11}) \\ & \in \ \text{gauge-like region}, \end{aligned} \tag{23}$$

which correspond, respectively, to values of $Y_{ee}$ and $v_\Delta$ close to their experimental upper limits. In light of the constraints from LHC measurements, the scan range of $m_{H^{\pm\pm}}$ is set as

$$m_{H^{\pm\pm}} \geqslant \begin{cases} 1100\ \text{GeV (Yukawa-like region)}, \\ 400\ \text{GeV (gauge-like region)}. \end{cases} \tag{24}$$

## III. DOUBLY CHARGED HIGGS PRODUCTION

Based on the HTM input parameters discussed above, we identify the dominant production mechanisms of $H^{\pm\pm}$ at lepton colliders in four collision modes: $e^+e^-$, $e^-e^-$, $e^-\gamma$, and $\gamma\gamma$. Among these, the $e^+e^-$ mode is typically the primary operating mode at lepton colliders, as it offers the highest integrated luminosity. High-energy photon beams in the initial state are generated via Compton backscattering, and their energy spectrum is given by [73]

$$\frac{1}{\sigma_c}\frac{\mathrm{d}\sigma_c}{\mathrm{d}y} = \frac{2\sigma_0}{x\sigma_c}\left[1 - y + \frac{1}{1-y} - \frac{4y}{x(1-y)} + \frac{4y^2}{x^2(1-y)^2}\right], \tag{25}$$

where $\sigma_c$ denotes the total Compton scattering cross section, and $y$ represents the fraction of the scattered photon energy relative to the incident electron beam energy. The

kinematic upper bound on $y$ is $y_{\max} = x/(1+x)$, where $x$ is a dimensionless parameter determined by the laser–electron configuration. In this work, we adopt $x = 4.8$ [74, 75], which corresponds to $y_{\max} \simeq 0.8$. Consequently, the maximum center-of-mass energies of the $\gamma\gamma$ and $e^-\gamma$ collision modes are approximately 80% and 90% of that of the $e^+e^-$ mode, respectively. For event generation, the HTM is implemented in `FeynRules` [76] to derive the relevant Feynman rules, which are then interfaced with `MadGraph5_aMC@NLO` [77] to generate $H^{\pm\pm}$ events.

• $e^+e^-$ **mode**:

For $\sqrt{s} > 2m_{H^{\pm\pm}}$, the production of $H^{\pm\pm}$ is dominated by Drell–Yan pair production, which is independent of $v_\Delta$ but exhibits mild sensitivity to $Y_{ee}$. When $\sqrt{s}$ falls below the $H^{\pm\pm}$ pair-production threshold, the dominant production mechanisms shift to $e^+e^- \to H^{\pm\pm}e^\mp e^\mp$ and $e^+e^- \to H^{\pm\pm}W^\mp W^\mp$. Both processes depend on $Y_{ee}$, but only the latter is sensitive to $v_\Delta$.

• $e^-e^-$ **mode**:

The leading channels in the $e^-e^-$ collision mode are $e^-e^- \to H^{--}\gamma$ and $e^-e^- \to H^{--}\nu_e\nu_e$. The former channel is independent of $v_\Delta$ but scales strongly with $Y_{ee}$, making it the dominant production channel in the Yukawa-like region. By contrast, the latter channel depends on both $v_\Delta$ and $Y_{ee}$ and dominates in the gauge-like region. For the benchmark parameters adopted in this analysis, the cross section for $H^{--}\nu_e\nu_e$ is significantly smaller than that of the photon-associated channel.

• $e^-\gamma$ **mode**:

In the Yukawa-like region, the process $e^-\gamma \to H^{--}e^+$ dominates the production of $H^{--}$, with a cross section that is independent of $v_\Delta$ and governed primarily by $Y_{ee}$. In the gauge-like region, the two principal production channels are $e^-\gamma \to H^{++}H^{--}e^-$ and $e^-\gamma \to H^{--}W^+\nu_e$. For the benchmark scenario considered here, the cross sections of these two channels are significantly smaller than that of $H^{--}e^+$ production in the Yukawa-like region.

• $\gamma\gamma$ **mode**:

In this collision mode, $H^{\pm\pm}$ is predominantly produced via the Drell–Yan process when kinematically allowed, with a cross section independent of both $v_\Delta$ and $Y_{ee}$. Below the $H^{\pm\pm}$ pair-production threshold, the doubly charged Higgs is primarily produced via $\gamma\gamma \to H^{\pm\pm}e^\mp e^\mp$ in the Yukawa-like region, with a cross section that depends on $Y_{ee}$ but is independent of $v_\Delta$. By contrast, in the gauge-like region, production mainly proceeds via $\gamma\gamma \to H^{\pm\pm}W^\mp W^\mp$, which is governed by $v_\Delta$ and insensitive to $Y_{ee}$.

For comparison, we also consider the dominant production mechanisms of the doubly charged Higgs boson at the LHC, including

$$\begin{aligned} &pp \to H^{\pm\pm}H^\mp + X, \qquad pp \to H^{++}H^{--} + X, \\ &pp \to H^{\pm\pm}jj + X, \qquad pp \to H^{\pm\pm}W^\mp + X. \end{aligned} \tag{26}$$

Among these, the associated production with a singly charged Higgs boson and Drell–Yan pair production are independent of $v_\Delta$ and $Y_{ee}$ and constitute the leading production modes at the LHC. The other two processes exhibit pronounced sensitivity to $v_\Delta$ and can attain sizable cross sections in the gauge-like region. In summary, all relevant production channels, together with their dependence on $v_\Delta$ and $Y_{ee}$, are listed in Table 2, and the corresponding dominant Feynman diagrams are shown in Fig. 2.

Figure 3 presents the production cross sections of the doubly charged Higgs boson as functions of its mass at the 3 TeV CLIC and the 14 TeV LHC. The two panels on the left illustrate the dominant production channels at BP1, where the production cross sections at CLIC are generally much larger than those at the LHC. At CLIC, the processes $e^-e^- \to H^{--}\gamma$ and $e^-\gamma \to H^{--}e^+$ yield the largest production cross sections. The cross section of the former increases with $m_{H^{\pm\pm}}$ because of the enhancement from the $s$-channel propagator $1/(s - m^2_{H^{\pm\pm}})$, whereas that of the latter decreases with increasing $m_{H^{\pm\pm}}$, primarily owing to phase-space suppression. Pair-production channels also yield appreciable cross sections, but they decrease rapidly with increasing $m_{H^{\pm\pm}}$ because of kinematic threshold effects. Overall, over most of the mass range, the production cross sections at CLIC are at least one order of magnitude larger than those at the LHC. The two panels on the right of Fig. 3 display the dominant produc-

**Table 2.** Dominant production channels of $H^{\pm\pm}$ and their dependence on $v_\Delta$ and $Y_{ee}$ at lepton and hadron colliders.

| Initial state | Final state | $v_\Delta$ | $Y_{ee}$ |
|---|---|---|---|
| $e^+e^-$ | $H^{++}H^{--}$ | | ✓ |
| | $H^{\pm\pm}e^\mp e^\mp$ | | ✓ |
| | $H^{\pm\pm}W^\mp W^\mp$ | ✓ | ✓ |
| $e^-e^-$ | $H^{--}\gamma$ | | ✓ |
| | $H^{--}\nu_e\nu_e$ | ✓ | ✓ |
| $e^-\gamma$ | $H^{--}e^+$ | | ✓ |
| | $H^{++}H^{--}e^-$ | | ✓ |
| | $H^{--}W^+\nu_e$ | ✓ | ✓ |
| $\gamma\gamma$ | $H^{++}H^{--}$ | | |
| | $H^{\pm\pm}e^\mp e^\mp$ | | ✓ |
| | $H^{\pm\pm}W^\mp W^\mp$ | ✓ | |
| $pp$ | $H^{\pm\pm}H^\mp$ | | |
| | $H^{++}H^{--}$ | | |
| | $H^{\pm\pm}jj$ | ✓ | |
| | $H^{\pm\pm}W^\mp$ | ✓ | |

CPC Accepted

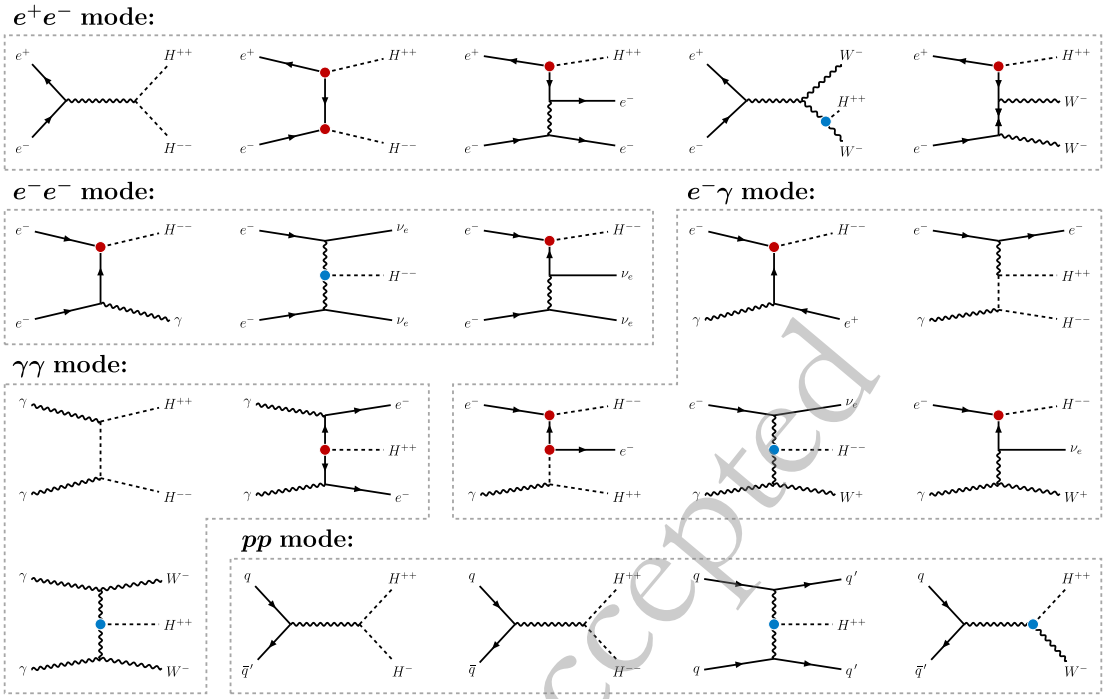



**Fig. 2.** (color online) Dominant Feynman diagrams for the production channels of the doubly charged Higgs boson. The red and blue dots denote the $H^{\pm\pm}e^{\mp}e^{\mp}$ Yukawa vertex and the $H^{\pm\pm}W^{\mp}W^{\mp}$ gauge vertex, respectively, with the corresponding couplings proportional to $Y_{ee}$ and $v_{\Delta}$.

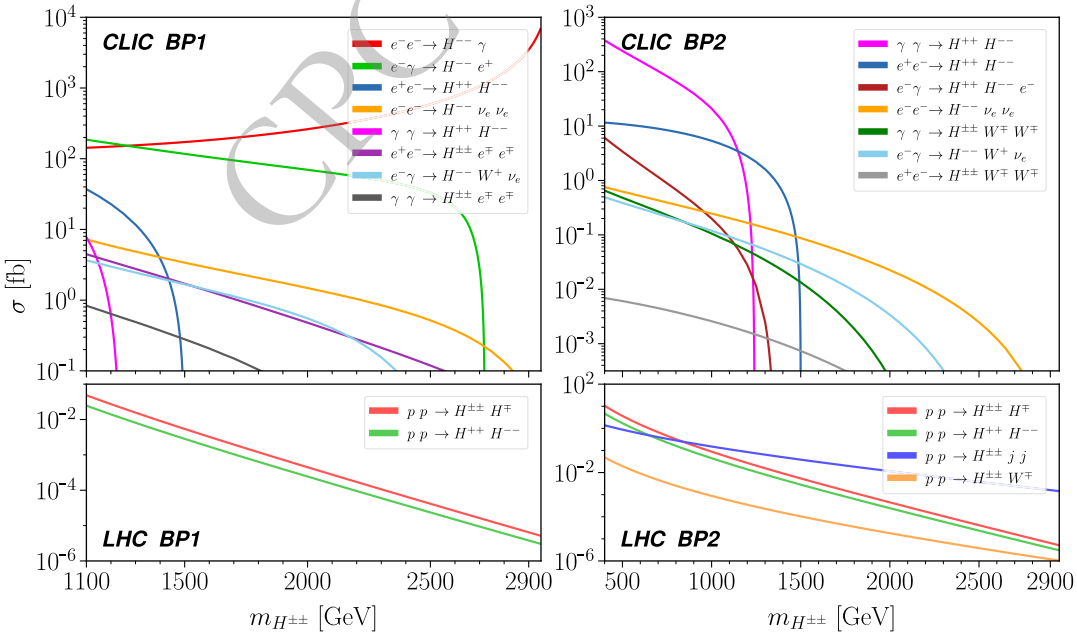



**Fig. 3.** (color online) Production cross sections of $H^{\pm\pm}$ as functions of $m_{H^{\pm\pm}}$ at the 3 TeV CLIC and the 14 TeV LHC for BP1 and BP2.

tion channels at BP2, where $H^{\pm\pm}$ pair production becomes the leading mechanism at CLIC. Nevertheless, its cross section is strongly constrained by kinematic thresholds and therefore decreases rapidly with increasing $m_{H^{\pm\pm}}$.

Based on the hierarchy of the production cross sections, we identify representative channels at CLIC for each benchmark point, BP1 and BP2,

$$\begin{aligned} &\text{BP1}: \ e^-e^- \to H^{--}\gamma, \qquad e^-\gamma \to H^{--}e^+, \\ &\text{BP2}: \ \gamma\gamma \to H^{++}H^{--}, \quad e^+e^- \to H^{++}H^{--}. \end{aligned} \tag{27}$$

which will be studied in detail in Sec.IV. In addition, we

CPC Accepted

will analyze $H^{\pm\pm}$ pair production at the 14 TeV LHC for both benchmark scenarios in Sec.V to compare the discovery potential of the doubly charged Higgs boson at different colliders.

## IV. DISCOVERY POTENTIAL AT CLIC

In this section, we present a detailed study of the discovery potential for doubly charged Higgs bosons at CLIC. Since the projected center-of-mass energy at CLIC Stage I is only 380 GeV, our analysis primarily uses data from CLIC Stage II ($\sqrt{s} = 1.5$ TeV) and Stage III ($\sqrt{s} = 3.0$ TeV), with integrated luminosities of 2.5 $ab^{-1}$ and 5.0 $ab^{-1}$, respectively [78]. These values correspond to the $e^+e^-$ collision mode; for the other three collision modes, we assume integrated luminosities of 25 $fb^{-1}$ at Stage II and 50 $fb^{-1}$ at Stage III.

Both signal and background events are generated using `MadGraph5_aMC@NLO` [77], with the decays of unstable particles handled by `MadSpin` [79]. Initial- and final-state radiation effects are simulated with `Pythia8` [80]. Detector effects, such as tracking efficiency and energy/momentum resolution, are incorporated through `Delphes` [81] using the CLIC detector configuration [82]. For lepton (electrons or muons, unless otherwise stated) and photon reconstruction, an isolation criterion is applied: the scalar sum of $p_T$ of particles within $\Delta R = 0.1$ around the reconstructed object must be less than 20% of its $p_T$. Final-state jets are reconstructed using the `FastJet` [83] package and clustered with the Valencia Linear Collider (VLC) algorithm [84, 85] in inclusive mode. If a $b$-jet is present in the final state, the 70% efficiency working point is used [82]. Beam-induced backgrounds (e.g., $\gamma\gamma \to$ hadrons) are simulated by applying additional energy smearing to the reconstructed jets. For the background analysis, the following baseline selection criteria are defined for the final-state objects:

$$\begin{aligned} &p_{T,\ell} > 10\ \text{GeV}, \quad p_{T,\gamma} > 10\ \text{GeV}, \quad p_{T,j} > 20\ \text{GeV}, \\ &|\eta_\ell| < 2.5, \quad |\eta_\gamma| < 2.5, \quad |\eta_j| < 5.0. \end{aligned} \tag{28}$$

The event selection is implemented in `MadAnalysis5` [86]. As illustrated in Fig. 1, $H^{\pm\pm}$ decays predominantly into same-sign lepton pairs in the Yukawa-like region and into same-sign $W$-boson pairs in the gauge-like region. In the background analysis, we adopt the following convention: if a scattering process involves an intermediate state, only the resonance associated with that state is considered; otherwise, it denotes the residual non-resonant contribution after all resonances have been subtracted.

### A. $e^-e^- \to H^{--}\gamma \to e^-e^-\gamma$ at BP1

As shown in the top-left panel of Fig. 3, $H^{--}\gamma$ associated production in $e^-e^-$ collisions is the dominant production channel in the Yukawa-like region. We therefore focus on this production mechanism and the subsequent decay $H^{--} \to e^-e^-$. The signal is required to contain two electrons and one photon in the final state, all of which must satisfy the baseline selection criteria. The major SM backgrounds are $e^-e^- \to e^-e^-\gamma$ and $e^-e^- \to W^-e^-\nu_e\gamma \to e^-\bar{\nu}_e e^-\nu_e\gamma$, with the former accounting for approximately 95% of the total background. Table 3 summarizes the numbers of signal and background events after the baseline selection, together with the corresponding statistical significances $\mathcal{S}$, defined as

$$\mathcal{S} = \frac{N_S}{\sqrt{N_S + N_B}}, \tag{29}$$

where $N_S$ and $N_B$ denote the expected numbers of signal and background events, respectively. For each representative value of $m_{H^{\pm\pm}}$, the expected numbers of signal and background events are both approximately of $O(10^3)$, resulting in a statistical significance well above $5\sigma$. As the signal cross section scales with $Y_{ee}^2$, the minimum $Y_{ee}$ required to achieve a $5\sigma$ significance can be inferred. Although these values lie well below the current upper limit from Bhabha scattering experiments, $Y_{ee} < 0.35$, additional kinematic cuts can further improve the discovery sensitivity, reducing the minimum $Y_{ee}$ required for a $5\sigma$ discovery.

Figure 4 presents selected kinematic distributions for the $e^-e^-\gamma$ final state at $\sqrt{s} = 3$ TeV CLIC after the baseline selection. Compared with the background, the signal exhibits a harder $p_{T,\gamma}$ distribution, and the pseudorapidity distribution of its leading electron is more concentrated in the central region. For the same-sign electron pair from the $H^{--}$ decay, the $\Delta R(e^-, e^-)$ distribution is shifted toward smaller values relative to that of the background, and the $M_{e^-e^-}$ distribution peaks around $m_{H^{\pm\pm}}$. Motivated by these differences in the kinematic distributions, we impose the following selection criteria on events passing the baseline selection:

**Table 3.** Event yields for the signal process $e^-e^- \to H^{--}\gamma \to e^-e^-\gamma$ and its background, together with the corresponding statistical significance and the minimum $Y_{ee}$ required for a $5\sigma$ discovery.

| $\sqrt{s}$/TeV | 1.5 | 3.0 | | | |
|---|---|---|---|---|---|
| | ($N_{\text{bkg}} = 11.8\times10^3$) | ($N_{\text{bkg}} = 7.49\times10^3$) | | | |
| $m_{H^{\pm\pm}}$/GeV | 1100 | 1100 | 1500 | 2000 | 2500 |
| $N_{\text{signal}}$ ($\times10^3$) | 22.4 | 4.38 | 5.42 | 8.40 | 19.0 |
| $\mathcal{S}$ | 121 | 40.2 | 47.7 | 66.7 | 117 |
| $Y_{ee}$ | 0.0551 | 0.112 | 0.100 | 0.0806 | 0.0536 |

CPC Accepted

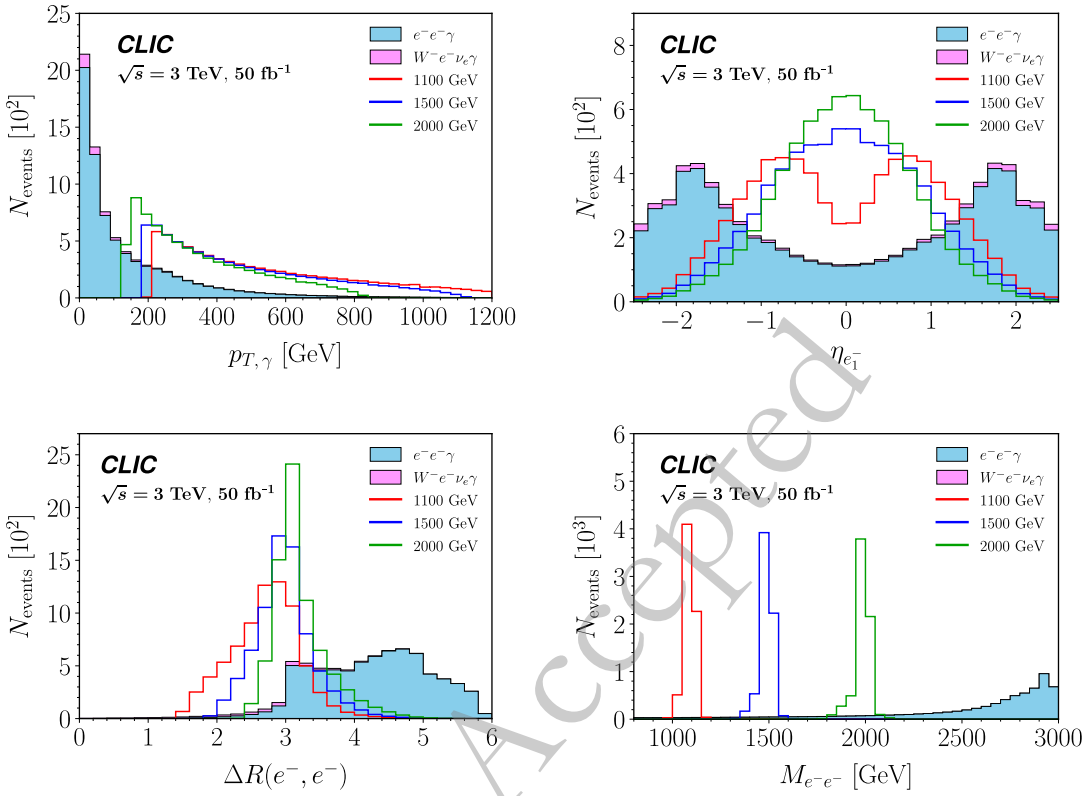



**Fig. 4.** (color online) Kinematic distributions for the signal process $e^-e^- \to H^{--}\gamma \to e^-e^-\gamma$ and its backgrounds at $\sqrt{s} = 3$ TeV CLIC. The signal yield is normalized to the total background yield.

$$p_{T,\gamma} > 50\,\text{GeV}, \quad |\eta_{e_1^-}| < 1.8, \quad \Delta R(e^-, e^-) < 4.5, \quad 0.9\,m_{H^{\pm\pm}} < M_{e^-e^-} < 1.1\,m_{H^{\pm\pm}}. \tag{30}$$

The resulting cutflow is presented in Table 4. After applying these selection cuts, more than 90% of the signal events are retained, while the background event yield is reduced to less than 15% of its original value. Accordingly, the minimum value of $Y_{ee}$ required for a $5\sigma$ discovery is reduced by approximately a factor of two. For Yukawa couplings in the range $Y_{ee} \in [0.03, 0.04]$, a doubly charged Higgs boson with a mass between 1100 and 2500 GeV could be discovered at future CLIC. This demonstrates that the $e^-e^-$ mode at CLIC provides excellent sensitivity for probing the doubly charged Higgs boson when it predominantly decays into a same-sign lepton pair.

### B. $e^-\gamma \to H^{--}e^+ \to e^-e^-e^+$ at BP1

In the Yukawa-like region, the process $e^-\gamma \to H^{--}e^+$ represents another major production channel for the doubly charged Higgs boson, with a cross section comparable to that of $e^-e^- \to H^{--}\gamma$ at low masses. For the signal process $e^-\gamma \to H^{--}e^+ \to e^-e^-e^+$, the event selection requires exactly three final-state electrons with a total electric charge of $-e$, all of which must satisfy the baseline selection criteria. The dominant SM backgrounds are

$$(1)e^+e^-e^-, \quad (2)W^+W^-e^-, \quad (3)W^-Z\nu_e, \quad (4)Ze^-. \tag{31}$$

Among these, the irreducible process $e^-\gamma \to e^+e^-e^-$ is the dominant contribution, accounting for approximately 70% of the total background. The processes $e^-\gamma \to W^+W^-e^-$ and $W^-Z\nu_e$ lead to the same final state as the signal through leptonic decays of the weak gauge bosons and constitute subleading backgrounds. By contrast, the $Ze^-$ background contributes the least, accounting for about 5% of the total. Notably, the process $e^-\gamma \to e^-jj$ has a sizable production cross section and may therefore be considered an SM background if the final-state jets are misidentified as an oppositely charged electron pair. However, with the electron isolation criterion applied, the probability of a jet being misidentified as an electron is well below $O(10^{-3})$, rendering this background negligible compared with those listed in Eq. (31).

After applying only the baseline selection criteria, the signal significance is sufficiently high. Table 5 presents the event yields for the signal and background, together with the corresponding signal significances, at CLIC Stage II and Stage III after the baseline selection. For each selected value of $m_{H^{\pm\pm}}$, both the signal and background yield roughly $10^3$ events, resulting in a statistical significance well above the $5\sigma$ threshold. The table also lists the minimal $Y_{ee}$ required to achieve a $5\sigma$ observa-

CPC Accepted

**Table 4.** Cutflow for the signal $e^-e^- \to H^{--}\gamma \to e^-e^-\gamma$ and its background at $\sqrt{s} = 1.5$ and 3 TeV CLIC, together with the minimum $Y_{ee}$ required for a $5\sigma$ discovery.

| $\sqrt{s}$/TeV | $m_{H^{\pm\pm}}$/GeV | quantity | baseline | $p_{T,\gamma}$ | $\eta_{e_1^-}$ | $\Delta R(e^-,e^-)$ | $M_{e^-e^-}$ |
|---|---|---|---|---|---|---|---|
| 1.5 | 1100 | $N_{\rm signal}$ | 22400 | 22200 | 21800 | 21700 | 21100 |
| | | $N_{\rm bkg}$ | 11800 | 5870 | 4020 | 3670 | 961 |
| | | $Y_{ee}$ | 0.0551 | 0.0467 | 0.0430 | 0.0422 | 0.0312 |
| 3.0 | 1100 | $N_{\rm signal}$ | 4380 | 4360 | 4150 | 4150 | 4090 |
| | | $N_{\rm bkg}$ | 7490 | 4350 | 2860 | 2530 | 84.4 |
| | | $Y_{ee}$ | 0.112 | 0.0981 | 0.0909 | 0.0883 | 0.0424 |
| | 1500 | $N_{\rm signal}$ | 5420 | 5400 | 5240 | 5240 | 5170 |
| | | $N_{\rm bkg}$ | 7490 | 4350 | 2860 | 2530 | 159 |
| | | $Y_{ee}$ | 0.100 | 0.0881 | 0.0809 | 0.0786 | 0.0427 |
| | 2000 | $N_{\rm signal}$ | 8400 | 8360 | 8190 | 8160 | 8060 |
| | | $N_{\rm bkg}$ | 7490 | 4350 | 2860 | 2530 | 351 |
| | | $Y_{ee}$ | 0.0806 | 0.0708 | 0.0647 | 0.0630 | 0.0403 |
| | 2500 | $N_{\rm signal}$ | 19000 | 18900 | 18600 | 18300 | 18100 |
| | | $N_{\rm bkg}$ | 7490 | 4350 | 2860 | 2530 | 960 |
| | | $Y_{ee}$ | 0.0536 | 0.0471 | 0.0430 | 0.0421 | 0.0337 |

tion within the mass range [1100, 2500] GeV, which in all cases lies below the current experimental upper limit.

Following the strategy adopted for the $e^-e^-$ channel, we further exploit the kinematic differences between the signal and background processes to suppress background contributions and enhance the discovery sensitivity. The relevant kinematic distributions are shown in Fig. 5. The transverse-momentum distribution of the leading electron is harder for the signal than for the background. Because the backscattered photon carries less energy than the electron beam, the $e^-\gamma$ center-of-mass frame is boosted along the electron-beam direction, shifting the $\eta_{e_1^-}$ distributions of both signal and background events toward the forward region. Within this overall shift, background events preferentially populate the far-forward region of the $\eta_{e_1^-}$ distribution, whereas the signal exhibits a broad peak at moderate $\eta_{e_1^-}$. In addition, the signal shows a clear resonance peak at $m_{H^{\pm\pm}}$ in the invariant-mass distribution of the same-sign electron pair. These kinematic differences motivate the following selection criteria:

**Table 5.** Same as Table 3, but for $e^-\gamma \to H^{--}e^+ \to e^-e^-e^+$.

| $\sqrt{s}$/TeV | 1.5 | 3.0 | | | |
|---|---|---|---|---|---|
| | ($N_{\rm bkg} = 1.82\times10^3$) | ($N_{\rm bkg} = 1.23\times10^3$) | | | |
| $m_{H^{\pm\pm}}$/GeV | 1100 | 1100 | 1500 | 2000 | 2500 |
| $N_{\rm signal}$ ($\times10^3$) | 3.42 | 5.56 | 3.65 | 2.21 | 1.03 |
| $\mathcal{S}$ | 47.2 | 67.5 | 52.2 | 37.7 | 21.7 |
| $Y_{ee}$ | 0.0900 | 0.0644 | 0.0795 | 0.102 | 0.150 |

$$p_{T,e_1^-} > 300\ {\rm GeV}, \quad -1.0 < \eta_{e_1^-} < 2.0,$$
$$0.9\, m_{H^{\pm\pm}} < M_{e^-e^-} < 1.1\, m_{H^{\pm\pm}}. \tag{32}$$

Table 6 presents the cutflow for the signal and background events. The selection cuts defined above retain approximately 90% of the signal events while suppressing the total background yield by more than 90%, with the mass-window requirement playing the dominant role in background rejection. Consequently, the minimum $Y_{ee}$ values required for a $5\sigma$ discovery are reduced by approximately a factor of two, falling in the range 0.04 – 0.07 at $\sqrt{s} = 3$ TeV for 1100 GeV $< m_{H^{\pm\pm}} <$ 2500 GeV. These results indicate that the channel $e^-\gamma \to H^{--}e^+ \to e^-e^-e^+$ is a promising and sensitive avenue for the discovery of the doubly charged Higgs boson when the Yukawa coupling to charged leptons is sufficiently large.

### C. $\gamma\gamma \to H^{++}H^{--} \to W^+W^+W^-W^-$ at BP2

In the gauge-like region, the dominant production mechanism for the doubly charged Higgs boson is pair production via $\gamma\gamma$ collisions, whenever kinematically allowed, as illustrated in the top-right panel of Fig. 3. The produced $H^{\pm\pm}$ bosons subsequently decay exclusively into same-sign $W$-boson pairs, leading to the signal process $\gamma\gamma \to H^{++}H^{--} \to W^+W^+W^-W^-$. Taking into account the $W$-boson decay branching fractions and the complexity of the relevant backgrounds, we focus on signal events featuring a same-sign dilepton (SSDL) in the final state, specifically $4W \to \ell^\pm\ell^\pm + 2\nu + 4q$, with $\ell = e,\mu$. To optimize

CPC Accepted

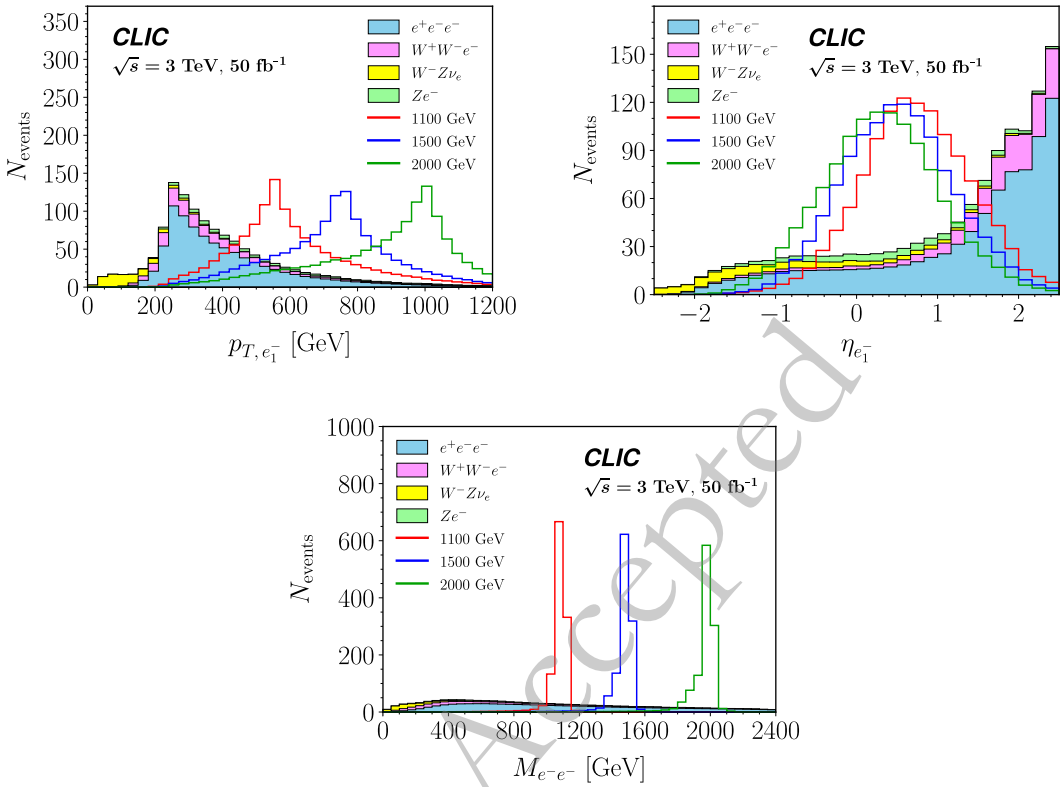



**Fig. 5.** (color online) Same as Fig. 4, but for $e^-\gamma \to H^{--}e^+ \to e^-e^-e^+$.

**Table 6.** Same as Table 4, but for $e^-\gamma \to H^{--}e^+ \to e^-e^-e^+$.

| $\sqrt{s}$/TeV | $m_{H^{\pm\pm}}$/GeV | quantity | baseline | $p_{T,e_1^-}$ | $\eta_{e_1^-}$ | $M_{e^-e^-}$ |
|---|---|---|---|---|---|---|
| 1.5 | 1100 | $N_{\rm signal}$ | 3420 | 3080 | 3070 | 2940 |
| | | $N_{\rm bkg}$ | 1820 | 296 | 289 | 45.9 |
| | | $Y_{ee}$ | 0.0900 | 0.0629 | 0.0627 | 0.0450 |
| 3.0 | 1100 | $N_{\rm signal}$ | 5560 | 5420 | 5300 | 5070 |
| | | $N_{\rm bkg}$ | 1230 | 758 | 592 | 75.6 |
| | | $Y_{ee}$ | 0.0644 | 0.0584 | 0.0558 | 0.0373 |
| | 1500 | $N_{\rm signal}$ | 3650 | 3610 | 3540 | 3380 |
| | | $N_{\rm bkg}$ | 1230 | 758 | 592 | 76.3 |
| | | $Y_{ee}$ | 0.0795 | 0.0715 | 0.0683 | 0.0458 |
| | 2000 | $N_{\rm signal}$ | 2210 | 2200 | 2120 | 2020 |
| | | $N_{\rm bkg}$ | 1230 | 758 | 592 | 54.7 |
| | | $Y_{ee}$ | 0.102 | 0.0916 | 0.0883 | 0.0559 |
| | 2500 | $N_{\rm signal}$ | 1030 | 1020 | 949 | 905 |
| | | $N_{\rm bkg}$ | 1230 | 758 | 592 | 22.1 |
| | | $Y_{ee}$ | 0.150 | 0.135 | 0.132 | 0.0728 |

signal selection based on the final-state topology, we require events to contain two same-sign leptons and at least three jets—excluding $b$-jets to suppress top-related backgrounds—*i.e.*, $\ell^\pm\ell^\pm + \geq 3j$. This semileptonic topology offers a favorable balance: it yields significantly higher statistics than the fully leptonic channel while avoiding the overwhelming multijet backgrounds associated with the fully hadronic channel. It should be noted that the de-

CPC Accepted

cay $4W \to \ell^+\ell^-\ell^\pm + 3\nu + 2q$ also contributes to the signal final state, accounting for approximately 10% of the total signal events. We identify the following dominant backgrounds for the $\ell^\pm\ell^\pm + \geq 3j$ final state:

$$(1)\ 4W,\quad (2)\ WWZ,\quad (3)\ t\bar{t},\quad (4)\ tbW,\quad (5)\ WWh. \tag{33}$$

The first two correspond to prompt lepton backgrounds, in which SSDLs arise directly from vector-boson decays. Contributions from both the $2\ell$ and $3\ell$ final states are included to ensure consistency with the signal treatment. These two processes constitute the dominant background. For the $t\bar{t}$ and $tbW$ backgrounds, the SSDL primarily consists of a prompt lepton from a $W$-boson decay and a non-prompt lepton originating from a $b$-hadron decay. For the $WWh$ background, contributions arise either from prompt production via $h \to VV^*$ decays or from non-prompt production via the $h \to b\bar{b}$ decay. Information related to the signal and background events is provided in Table 7. In the low-mass regime ($m_{H^{\pm\pm}} \lesssim 600$ GeV), the statistical significance substantially exceeds the $5\sigma$ discovery threshold. Because the signal significance is relatively low in the high-mass region, a set of kinematic cuts is introduced to better discriminate the signal from the background.

**Table 7.** Event yields for the signal $\gamma\gamma \to H^{++}H^{--} \to 4W \to \ell^\pm\ell^\pm + \geq 3j$ and the background, together with the corresponding statistical significance.

| $\sqrt{s}$/TeV | 1.5 | 3.0 | | | |
|---|---|---|---|---|---|
| | ($N_{\rm bkg}$ = 49.1) | ($N_{\rm bkg}$ = 202) | | | |
| $m_{H^{\pm\pm}}$/GeV | 400 | 400 | 600 | 800 | 1000 |
| $N_{\rm signal}$ | 275 | 664 | 279 | 95.0 | 23.9 |
| $\mathcal{S}$ | 15.3 | 22.6 | 12.7 | 5.51 | 1.59 |

Figure 6 shows selected kinematic distributions for the $\ell^\pm\ell^\pm + \geq 3j$ final state at $\sqrt{s} = 3$ TeV CLIC after the baseline selection, including the transverse momentum and pseudorapidity of the leading lepton, the invariant mass of the three leading jets, and the $S_T$ variable, defined as

$$S_T = \sum_{j\in\text{jets}} p_{T,j} + \not{p}_T, \tag{34}$$

where the scalar sum runs over all reconstructed jets, and $\not{p}_T$ denotes the missing transverse momentum. As illustrated in the figure, the signal and background are well separated in these kinematic distributions. To improve the signal significance in the high-mass region, we therefore apply the following kinematic cuts:

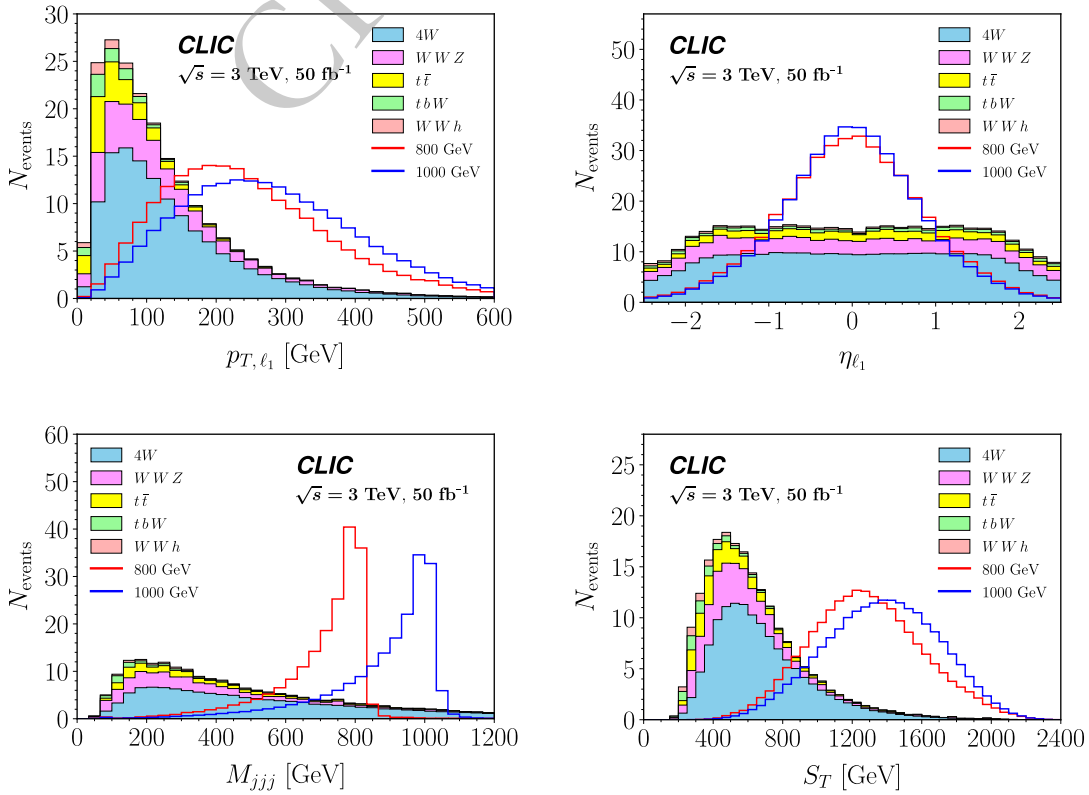



**Fig. 6.** (color online) Same as Fig. 4, but for $\gamma\gamma \to H^{++}H^{--} \to 4W \to \ell^\pm\ell^\pm + \geq 3j$.

CPC Accepted

$$p_{T,\ell_1} > 120\ \text{GeV}, \quad |\eta_{\ell_1}| < 1.5,$$
$$M_{jjj} > 500\ \text{GeV}, \quad S_T > 800\ \text{GeV}. \tag{35}$$

The cutflow for signal and background events is presented in Table 8. After applying the optimized selection criteria in Eq.(35), more than 70% of the signal events are retained, while the total background is reduced to below 10% of its yield after the baseline selection. For a doubly charged Higgs boson with a mass of around 1 TeV, approximately 20 signal events are expected at $\sqrt{s} = 3$ TeV CLIC after the optimized event selection, assuming an integrated luminosity of 50 $\text{fb}^{-1}$. These results demonstrate that the $\gamma\gamma$ collision mode at CLIC provides a promising experimental platform for searching for doubly charged Higgs bosons below the TeV scale. For low-mass doubly charged Higgs bosons, although the signal significance is already sufficiently high, it can still be improved further by refining the kinematic cuts in Eq.(35) as follows:

$$p_{T,\ell_1} > 25\ \text{GeV}, \quad |\eta_{\ell_1}| < 2.5,$$
$$M_{jjj} > 260\ \text{GeV}, \quad S_T > 660\ \text{GeV}. \tag{36}$$

The corresponding cutflow for the representative mass point $m_{H^{\pm\pm}} = 600$ GeV is presented in Table 8.

### D. $e^+e^- \to H^{++}H^{--} \to W^+W^+W^-W^-$ at BP2

In addition to $\gamma\gamma \to H^{++}H^{--}$ studied in subsection IV C, the $e^+e^-$ collision mode provides another major production mechanism for doubly charged Higgs boson pairs at lepton colliders in the gauge-like region, as shown in the top-right panel of Fig. 3. Since $H^{\pm\pm}$ predominantly decays into same-sign $W$ boson pairs in this region, the corresponding signal process is $e^+e^- \to H^{++}H^{--} \to W^+W^+W^-W^-$. Analogous to the $\gamma\gamma \to H^{++}H^{--} \to 4W$ signal process studied in the previous subsection, we focus exclusively on the $\ell^\pm\ell^\pm + \geq 3j$ final state from the $4W$ system to investigate the discovery potential of the doubly charged Higgs boson in $e^+e^-$ collisions. Although the $e^+e^-$ collision mode probes the same final state, its background composition differs substantially from that of the $\gamma\gamma$ mode, primarily because of its fixed center-of-mass energy and the dominance of the $s$-channel production mechanism. Consequently, the dominant backgrounds in the $e^+e^-$ mode are

$$\begin{aligned}&(1)\ W^+W^-\ell^+\ell^-, \quad (2)\ W^+W^-W^\pm\ell^\mp\nu, \quad (3)\ W^\pm Z\ell^\mp\nu,\\ &(4)\ W^+W^-Z\ell^+\ell^-, \quad (5)\ W^+W^+W^-W^-, \quad (6)\ W^+W^-Z,\\ &(7)\ W^+W^-ZZ.\end{aligned} \tag{37}$$

All these backgrounds arise from prompt production. The SSDL signature typically consists of one non-resonant lepton and one lepton from a vector-boson decay, with contributions from jet misidentification being negligible. The first two backgrounds are dominant, accounting for approximately 85% of the total, whereas the last three, which arise solely from resonant production, contribute only a minor fraction, less than 5%.

Table 9 presents the expected numbers of signal and background events, together with the corresponding signal significance, for five representative mass points in the range of [400, 1200] GeV. The results show that, in the low-mass region, the signal significance substantially exceeds $10\sigma$. It is worth noting that the mass of the doubly charged Higgs boson introduces two competing effects. In high-energy collisions, the Lorentz boost of an unstable particle typically collimates its decay products, which in turn reduces the efficiency of both object reconstruction and event selection. For the $e^+e^- \to H^{\pm\pm}H^{\mp\mp} \to 4W$ process studied at 3 TeV CLIC, an increase in $m_{H^{\pm\pm}}$ leads to a more balanced distribution of the energies and directions of the four $W$ bosons. This change weakens the overall effect of the Lorentz boost, thereby mitigating the

CPC Accepted

**Table 8.** Cutflow for the signal $\gamma\gamma \to H^{++}H^{--} \to 4W \to \ell^\pm\ell^\pm + \geq 3j$ and its background at $\sqrt{s} = 3$ TeV CLIC, together with the corresponding statistical significance.

| | $m_{H^{\pm\pm}}$/GeV | quantity | baseline | $p_{T,\ell_1}$ | $\eta_{\ell_1}$ | $M_{jjj}$ | $S_T$ |
|---|---|---|---|---|---|---|---|
| high-mass | $N_{\text{bkg}}$ | | 202 | 79.2 | 54.9 | 23.2 | 13.9 |
| | 1000 | $N_{\text{signal}}$ | 23.9 | 21.6 | 21.1 | 20.2 | 19.8 |
| | | $\mathcal{S}$ | 1.59 | 2.15 | 2.42 | 3.07 | 3.41 |
| | 800 | $N_{\text{signal}}$ | 95.0 | 81.3 | 79.2 | 72.4 | 70.6 |
| | | $\mathcal{S}$ | 5.51 | 6.42 | 6.84 | 7.40 | 7.68 |
| low-mass | $N_{\text{bkg}}$ | | 202 | 191 | 191 | 134 | 59.7 |
| | 600 | $N_{\text{signal}}$ | 279 | 278 | 278 | 271 | 257 |
| | | $\mathcal{S}$ | 12.7 | 12.8 | 12.8 | 13.5 | 14.4 |

**Table 9.** Same as Table 7, but for $e^+e^- \to H^{++}H^{--} \to 4W \to \ell^\pm\ell^\pm + \geq 3j$.

| $\sqrt{s}$/TeV | 1.5 | | 3.0 | | | | |
|---|---|---|---|---|---|---|---|
| | ($N_{\rm bkg} = 1.49\times10^3$) | | ($N_{\rm bkg} = 4.32\times10^3$) | | | | |
| $m_{H^{\pm\pm}}$/GeV | 400 | 600 | 400 | 600 | 800 | 1000 | 1200 |
| $N_{\rm signal}$ ($\times10^3$) | 2.57 | 1.04 | 0.954 | 1.05 | 0.880 | 0.588 | 0.258 |
| $\mathcal{S}$ | 40.3 | 20.7 | 13.1 | 14.3 | 12.2 | 8.39 | 3.81 |

loss in event reconstruction and selection efficiency. Conversely, the production cross section of this process decreases with increasing $m_{H^{\pm\pm}}$ because of the phase-space suppression of the doubly charged Higgs pair. The interplay between these two effects yields a maximum signal significance at an intermediate value of $m_{H^{\pm\pm}}$, around 600 GeV.

To enhance the modest signal significance near the pair-production threshold at 3 TeV CLIC, a set of cuts on kinematic variables is introduced to improve signal–background discrimination. These variables include

(1)$\not{p}_T$: the missing transverse momentum;

(2)$\Delta R(\ell,\ell)$: the angular separation between the same-sign leptons;

(3)$\Delta\phi(\ell\ell,\not{p}_T)$: the azimuthal angle difference between the SSDL system and$\not{p}_T$;

(4) $S_T$: the scalar sum of the jet transverse momenta and $\not{p}_T$.

Their distributions for the signal and background processes are shown in Fig. 7, from which we define the following event selection criteria:

1. Signal events are characterized by larger $\not{p}_T$, and thus we require $\not{p}_T > 150$ GeV;

2. The same-sign lepton pair from $H^{\pm\pm}$ decays is typically more collimated, motivating the requirement $\Delta R(\ell,\ell) < 3$;

3. In signal events, the transverse momentum of the SSDL system typically aligns with $\not{p}_T$, thereby motivating the requirement $|\Delta\phi(\ell\ell,\not{p}_T)| < 1.5$;

4. The jets in signal events originate from the decays of the doubly charged Higgs bosons and typically produce larger values of $S_T$; therefore, we impose the requirement $S_T > 1500$ GeV.

Table 10 details the cutflow of signal and background yields, along with the resulting significance. The requirements on $\Delta\phi(\ell\ell,\not{p}_T)$ and $S_T$ provide the most sig-

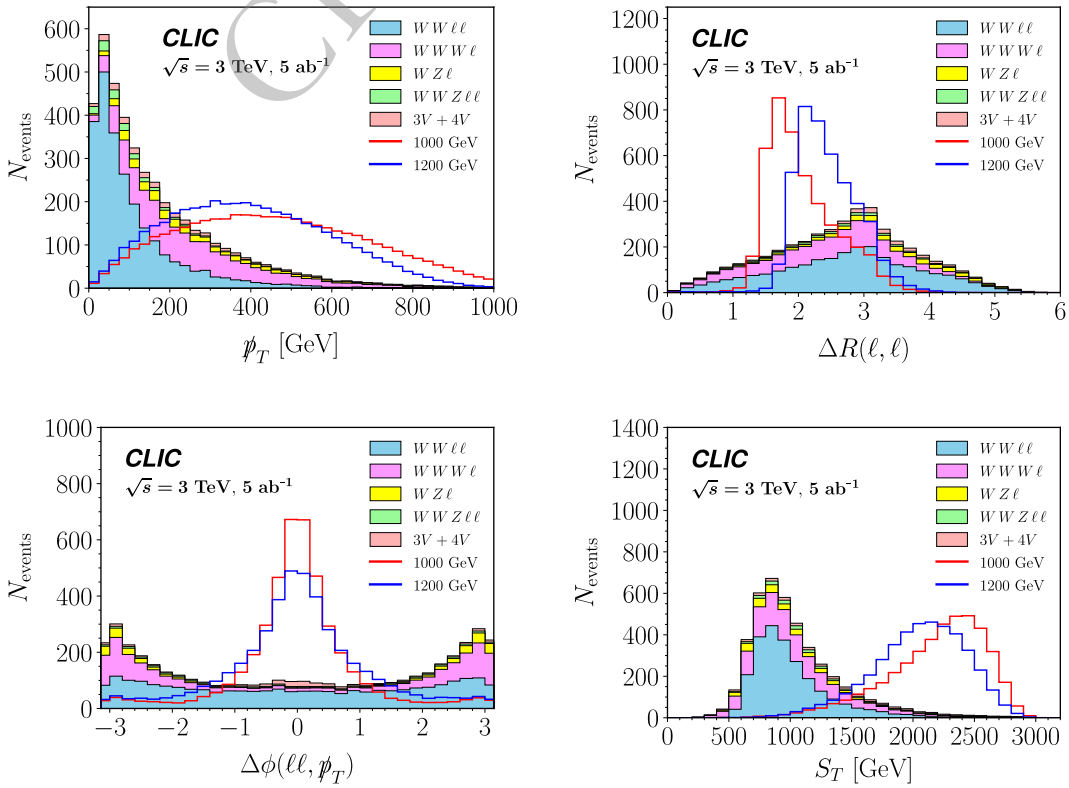



**Fig. 7.** (color online) Same as Fig. 4, but for $e^+e^- \to H^{++}H^{--} \to 4W \to \ell^\pm\ell^\pm + \geq 3j$.

CPC Accepted

nificant improvement in signal significance, consistent with the distributions shown in Fig. 7. The final results indicate that, even for $m_{H^{\pm\pm}} = 1200$ GeV, the signal significance exceeds $10\sigma$. This demonstrates that the $e^+e^-$ mode offers strong sensitivity to the doubly charged Higgs boson and covers nearly the entire kinematically accessible mass range. Compared with the $\gamma\gamma$ collision mode, the $e^+e^-$ mode yields roughly an order of magnitude more signal events at $m_{H^{\pm\pm}} = 1000$ GeV, primarily due to its higher integrated luminosity. At the same integrated luminosity, however, the $\gamma\gamma$ mode exhibits superior performance. For instance, at an integrated luminosity of 50 fb$^{-1}$ and for $m_{H^{\pm\pm}} = 1000$ GeV, the $e^+e^-$ mode retains only about 4 signal events, whereas the $\gamma\gamma$ mode yields approximately 19 after the optimized event selection criteria are applied.

## V. DISCOVERY POTENTIAL AT 14 TEV HL-LHC

For comparison, we investigate the discovery potential of the doubly charged Higgs boson at the 14 TeV HL-LHC with an integrated luminosity of 3 ab$^{-1}$. The signal process under consideration is Drell–Yan pair production, $pp \to H^{\pm\pm}H^{\mp\mp}$. The analysis is performed separately in the Yukawa-like and gauge-like regions. Both signal and background processes are simulated using the same computational framework as that developed for the CLIC study. Events are generated at the matrix-element level with up to two partons and subsequently matched to the parton shower using `Pythia8`. To suppress the more challenging background at hadron colliders, a tighter lepton isolation criterion is imposed: the scalar sum of the transverse momenta of all particles within a cone of radius $R = 0.5$ around the lepton, excluding the lepton itself, is required to be less than 12% of the lepton transverse momentum. Jets in the final state are reconstructed using the anti-$k_t$ algorithm with a radius parameter of $R = 0.4$. The baseline selection applied to final-state objects is identical to that used in the CLIC analysis, as defined in Eq. (28).

### A. $pp \to H^{++}H^{--} \to e^+e^+e^-e^-$ at BP1

In the Yukawa-like region, the $H^{\pm\pm}$ boson predominantly decays into same-sign lepton pairs. Under the single-flavor-dominance hypothesis, the signal process considered here is $pp \to H^{++}H^{--} \to e^+e^+e^-e^-$. At BP1, the pair-production cross section of $H^{\pm\pm}$ at the 14 TeV LHC is approximately four orders of magnitude smaller, or possibly even more, depending on the doubly charged Higgs mass, than those of the dominant production processes at CLIC. Nonetheless, owing to the clean four-lepton final state and the high integrated luminosity, a substantial signal significance is still expected.

At hadron colliders, backgrounds are typically much larger than those at lepton colliders. By requiring a final state with four electrons that satisfy the baseline selection criteria, the major backgrounds can be classified into three distinct categories:

• **Prompt lepton backgrounds**: including $ZZ$, $Z\ell^+\ell^-$, $\ell^+\ell^-\ell^+\ell^-$, $VVZ$ ($V = W, Z$), and $t\bar{t}Z$. In all cases, the vector bosons decay leptonically to electrons or $\tau$ leptons, and the $\tau$ leptons subsequently undergo cascade decays to electrons.

• **Fake lepton backgrounds**: originating from $WV$+jets and $t\bar{t}$ events, in which at least one electron is misidentified, for example from jets or $b$-hadrons.

• **$\gamma$-conversion backgrounds**: for example, the Drell–Yan process $pp \to Z/\gamma^* \to \ell^+\ell^-$, in which an additional electron–positron pair is produced through the conversion of an extra photon radiated from either the initial or final state.

Among these backgrounds, $\gamma$ conversion constitutes the dominant contribution, accounting for approximately 80% of the total. Resonant $ZZ$ production is the subleading background, contributing about 10%, while all other backgrounds remain relatively minor.

After applying the baseline event selection criteria, the background still overwhelmingly dominates over the signal. Owing to the relatively large mass of the doubly charged Higgs boson in the Yukawa-like scenario, the signal and background exhibit clearly distinct invariant-mass distributions for both same-sign and opposite-sign electron pairs, as illustrated in Fig. 8. For background events, the invariant mass of the leading opposite-sign

**Table 10.** Same as Table 8, but for $e^+e^- \to H^{++}H^{--} \to 4W \to \ell^\pm\ell^\pm + \geq 3j$.

| $m_{H^{\pm\pm}}$/GeV | quantity | baseline | $\not{p}_T$ | $\Delta R(\ell,\ell)$ | $\Delta\phi(\ell\ell,\not{p}_T)$ | $S_T$ |
|---|---|---|---|---|---|---|
| | $N_{\rm bkg}$ | 4320 | 1850 | 1060 | 216 | 64.2 |
| 1000 | $N_{\rm signal}$ | 588 | 539 | 504 | 461 | 448 |
| | $\mathcal{S}$ | 8.39 | 11.0 | 12.7 | 17.7 | 19.8 |
| 1200 | $N_{\rm signal}$ | 258 | 231 | 202 | 172 | 165 |
| | $\mathcal{S}$ | 3.81 | 5.06 | 5.69 | 8.73 | 10.9 |

CPC Accepted

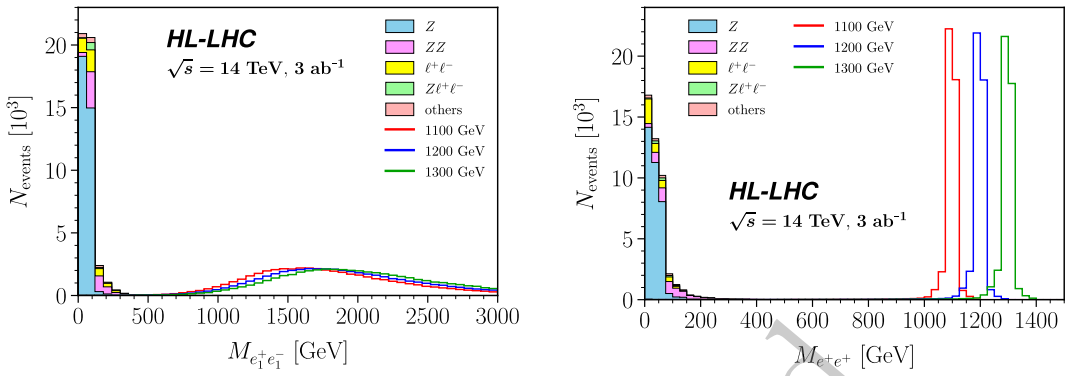



**Fig. 8.** (color online) Kinematic distributions for the signal process $pp \to H^{++}H^{--} \to e^+e^+e^-e^-$ and its backgrounds at the 14 TeV HL-LHC. The signal yield is normalized to the total background yield.

electron pair, $M_{e_1^+e_1^-}$, together with that of the same-sign electron pairs, such as $M_{e^+e^+}$, is concentrated in the low-mass region. In contrast, for signal events, $M_{e_1^+e_1^-}$ predominantly lies in the higher-mass region, while $M_{e^+e^+}$ exhibits a distinct peak near the doubly charged Higgs mass. Therefore, we introduce the following additional selection criteria on top of the baseline requirements:

$$M_{e_1^+e_1^-} > 500\,\text{GeV}, \qquad M_{e^\pm e^\pm} > 800\,\text{GeV}, \tag{38}$$

which effectively suppresses the background. Table 11 summarizes the signal and background event yields after each stage of the cutflow (baseline, $M_{e_1^+e_1^-}$, and $M_{e^\pm e^\pm}$), together with the corresponding statistical significance. At the HL-LHC, with an integrated luminosity of 3 ab$^{-1}$, a doubly charged Higgs boson with a mass of 1.1 TeV is expected to produce approximately 19 signal events, corresponding to a discovery potential slightly above $4\sigma$. In the Yukawa-like region, the small signal production cross section limits the HL-LHC sensitivity to a relatively narrow mass window for the doubly charged Higgs boson. Therefore, CLIC offers greater discovery potential than the HL-LHC for doubly charged Higgs bosons in the Yukawa-like scenario.

**Table 11.** Cutflow for the signal process $pp \to H^{++}H^{--} \to e^+e^+e^-e^-$ and the background at the 14 TeV HL-LHC, together with the corresponding significance.

| $m_{H^{\pm\pm}}$/GeV | quantity | baseline | $M_{e_1^+e_1^-}$ | $M_{e^\pm e^\pm}$ |
|---|---|---|---|---|
| | $N_{\rm bkg}$ | 45800 | 70.2 | 1.32 |
| 1100 | $N_{\rm signal}$ | 19.5 | 19.5 | 19.1 |
| | $\mathcal{S}$ | 0.0913 | 2.06 | 4.23 |
| 1200 | $N_{\rm signal}$ | 11.0 | 11.0 | 10.8 |
| | $\mathcal{S}$ | 0.0516 | 1.22 | 3.11 |
| 1300 | $N_{\rm signal}$ | 6.31 | 6.30 | 6.21 |
| | $\mathcal{S}$ | 0.0295 | 0.720 | 2.26 |

### B. $pp \to H^{++}H^{--} \to W^+W^+W^-W^-$ at BP2

In the gauge-like region, $H^{\pm\pm}$ predominantly decays into same-sign $W$-boson pairs. In this subsection, we investigate the process $pp \to H^{++}H^{--} \to W^+W^+W^-W^-$ at BP2 to evaluate the discovery potential of the doubly charged Higgs boson through its bosonic decay at the 14 TeV HL-LHC. Following the event selection strategy of the CLIC $4W$ analysis, we target the final state containing a same-sign lepton pair and at least three jets (excluding $b$-jets). The signal events arise primarily from $4W \to \ell^\pm\ell^\pm + 2\nu + 4q$, with a smaller contribution from $4W \to \ell^+\ell^-\ell^\pm + 3\nu + 2q$. Here, $\ell$ denotes an electron or a muon. Accordingly, the dominant backgrounds can be classified into two categories:

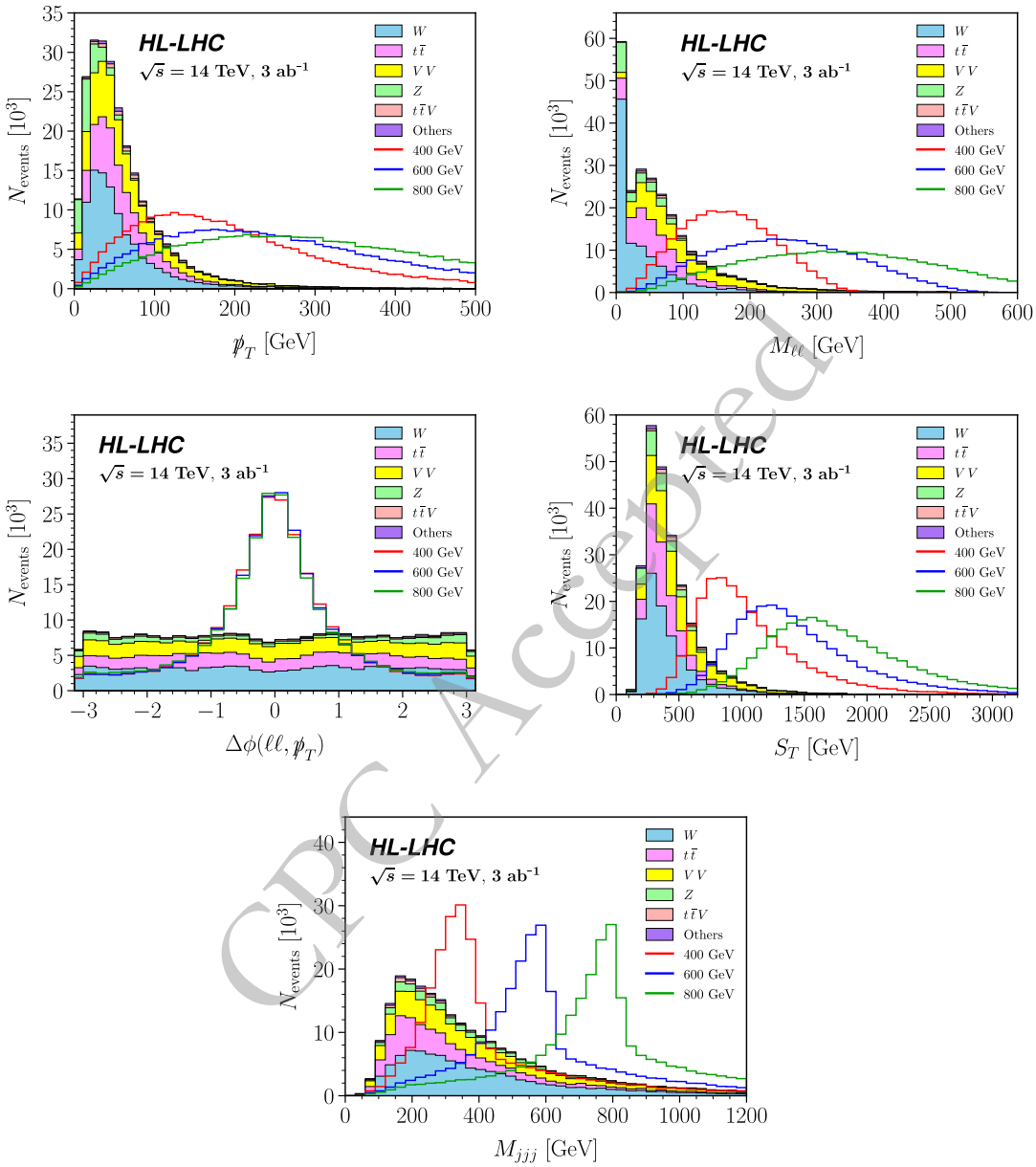
- **Prompt lepton backgrounds**: This category includes multiboson, $t\bar{t}V$, and $Vh$ ($h \to VV^*$) processes. Here, SSDLs originate from the leptonic decays of vector bosons, with $WZ \to \ell\nu\ell^+\ell^-$ providing the dominant contribution. $ZZ$, $t\bar{t}W$, and same-sign $W$-boson pair production also contribute noticeably. Other processes, including triboson and $Vh$ production, contribute only marginally because of their relatively small production cross sections and the tendency of their final states to contain more than two leptons, which leads to efficient rejection by the baseline selection.

- **Fake lepton backgrounds**: originating from $V$+jets and $t\bar{t}$ events.

In these backgrounds, at least one lepton arises from jet-to-lepton misidentification. Although the misidentification rate is small, the very large production cross sections of these processes result in more background events than prompt production. Among these processes, $W$+jets is the dominant contributor, followed by $t\bar{t}$, while $Z$+jets makes a comparatively smaller contribution.

In addition to the aforementioned backgrounds, events with charge misidentification may also contribute as a potential background. Studies reported in Ref. [59] indicate that, after the final event selection, the contribu-

CPC Accepted




CPC Accepted

**Fig. 9.** (color online) Same as Fig. 8, but for $pp \to H^{++}H^{--} \to 4W \to \ell^{\pm}\ell^{\pm} + \geq 3j$.

tion from this type of background is negligible. Moreover, with the exceptional tracking performance anticipated at the HL-LHC, the charge misidentification rate can be reduced to an exceedingly low level. As a result, this background is not considered in the current analysis.

After the baseline event selection, background events overwhelmingly dominate, exceeding the signal yield by three to four orders of magnitude. We therefore further compare several characteristic kinematic distributions of the signal and background processes and exploit their differences to achieve more efficient background suppression and consequently enhance the signal significance. As shown in Fig. 9, these discriminating variables include the invariant masses of the final-state lepton pair and the three leading jets, $M_{\ell\ell}$ and $M_{jjj}$, as well as $\not{p}_T$, $\Delta\phi(\ell\ell, \not{p}_T)$, and $S_T$. Owing to the large mass of the doubly charged Higgs boson, energy- and momentum-related kinematic variables, such as $\not{p}_T$, $M_{\ell\ell}$, $S_T$, and $M_{jjj}$, take larger values in signal events. Both the $S_T$ and $M_{jjj}$ distributions exhibit a strong dependence on $m_{H^{\pm\pm}}$: $S_T$ features a pronounced peak around $2m_{H^{\pm\pm}}$, while $M_{jjj}$ shows a peak that falls sharply near $m_{H^{\pm\pm}}$, indicating that these leading jets predominantly originate from the decay of $H^{\pm\pm}$. Motivated by these kinematic features, we implement the following optimized selection criteria to improve the signal significance:

$$\begin{aligned} &\not{p}_T > 120\,\text{GeV}, \quad M_{\ell\ell} > 80\,\text{GeV}, \quad S_T > 2m_{H^{\pm\pm}}, \\ &3/4\,m_{H^{\pm\pm}} < M_{jjj} < m_{H^{\pm\pm}} + 50\,\text{GeV}. \end{aligned} \tag{39}$$

**Table 12.** Same as Table 11, but for $pp \to H^{++}H^{--} \to 4W \to \ell^{\pm}\ell^{\pm} + \geq 3j$.

| $m_{H^{\pm\pm}}$/GeV | quantity | baseline | $\not{p}_T$ | $M_{\ell\ell}$ | $S_T$ | $M_{jjj}$ |
|---|---|---|---|---|---|---|
| 400 | $N_{\rm signal}$ | 399 | 283 | 247 | 200 | 90.2 |
| | $N_{\rm bkg}$ | $2.46\times10^5$ | $2.42\times10^4$ | $9.09\times10^3$ | $4.13\times10^3$ | 647 |
| | $\mathcal{S}$ | 0.804 | 1.81 | 2.56 | 3.04 | 3.32 |
| 600 | $N_{\rm signal}$ | 68.0 | 56.4 | 54.2 | 37.6 | 18.7 |
| | $N_{\rm bkg}$ | $2.46\times10^5$ | $2.42\times10^4$ | $9.09\times10^3$ | $1.30\times10^3$ | 180 |
| | $\mathcal{S}$ | 0.137 | 0.362 | 0.567 | 1.03 | 1.33 |
| 800 | $N_{\rm signal}$ | 14.6 | 13.0 | 12.8 | 7.74 | 3.62 |
| | $N_{\rm bkg}$ | $2.46\times10^5$ | $2.42\times10^4$ | $9.09\times10^3$ | 431 | 65.3 |
| | $\mathcal{S}$ | 0.0294 | 0.0835 | 0.134 | 0.370 | 0.436 |

Here, the upper bound of the $M_{jjj}$ selection window includes an additional 50 GeV margin to account for the broadening of the signal peak caused by finite jet energy resolution. Despite the substantial difference in the $\Delta\phi(\ell\ell, \not{p}_T)$ distributions between the signal and background, no cut is imposed on $\Delta\phi(\ell\ell, \not{p}_T)$ because of its correlation with $\not{p}_T$ and $M_{\ell\ell}$. Once cuts on $\not{p}_T$ and $M_{\ell\ell}$ are applied, its discriminating power becomes largely redundant.

The cutflow of the signal and background yields, together with the corresponding significance, is summarized in Table 12. It is evident that the selection efficiencies for signal and background events exhibit distinctly different dependences on the doubly charged Higgs mass. For the signal, the efficiency remains relatively stable across $m_{H^{\pm\pm}}$, at roughly 1/4. In contrast, for the background, the selection efficiency decreases as $m_{H^{\pm\pm}}$ increases. For instance, as $m_{H^{\pm\pm}}$ increases from 400 GeV to 600 GeV, the efficiency of the event selection criteria in Eq. (39) for the background decreases from approximately 3‰ to below 1‰. Assuming an integrated luminosity of 3 ab$^{-1}$, the expected statistical significance is approximately $3\sigma$ at $m_{H^{\pm\pm}} = 400$ GeV and decreases significantly with increasing $m_{H^{\pm\pm}}$. This behavior is primarily driven by the rapidly decreasing production cross section as $m_{H^{\pm\pm}}$ increases, as shown in the bottom-right panel of Fig. 3. In comparison, the 3 TeV CLIC offers substantial discovery potential for a TeV-scale doubly charged Higgs boson in the gauge-like scenario.

Based on the HL-LHC analyses presented above and the CLIC analyses in Section IV, we compare the prospects for probing doubly charged Higgs bosons at the two colliders. In the Yukawa-like region, the HL-LHC can probe $m_{H^{\pm\pm}} \lesssim 1.2$ TeV at the $3\sigma$ level, whereas the CLIC analyses maintain a statistical significance of at least $5\sigma$ across the entire 1.1 – 2.5 TeV mass range. In the gauge-like region, the HL-LHC is expected to achieve a statistical significance of approximately $3\sigma$ only near the lower end of the mass range considered. By contrast, the CLIC $\gamma\gamma$ mode maintains a significance of at least $5\sigma$ up to $m_{H^{\pm\pm}} \approx 800$ GeV, while the $e^+e^-$ mode achieves a significance exceeding $5\sigma$ for all benchmark masses investigated up to 1.2 TeV. Overall, CLIC substantially extends the discovery reach in both parameter regions, achieving a significance of at least $5\sigma$ over a much broader mass range than that accessible at the HL-LHC at the $3\sigma$ level.

## VI. SUMMARY

In this work, we present a comprehensive analysis of the discovery potential of the doubly charged Higgs boson at CLIC in the $e^-e^-$, $e^-\gamma$, $\gamma\gamma$, and $e^+e^-$ collision modes within the Higgs triplet model. In the Yukawa-like region, the dominant production mechanism for the doubly charged Higgs boson at CLIC is single production in $e^-e^-$ and $e^-\gamma$ collisions, followed by decay into a same-sign lepton pair. These two production modes can achieve a $5\sigma$ discovery sensitivity for a TeV-scale doubly charged Higgs boson, requiring only $Y_{ee} \sim 0.03 - 0.07$ under the single-flavor-dominance hypothesis, well below the current experimental limit of $Y_{ee} < 0.35$. In contrast, in the gauge-like region, pair production in $\gamma\gamma$ and $e^+e^-$ collisions dominates, with subsequent decay into a same-sign $W$ boson pair. Based on the $\ell^{\pm}\ell^{\pm} + \geq 3j$ event selection and assuming an integrated luminosity of 50 fb$^{-1}$, the $\gamma\gamma$ mode can achieve a $5\sigma$ discovery significance for $H^{\pm\pm}$ with $m_{H^{\pm\pm}} \lesssim 800$ GeV. In the $e^+e^-$ mode, the production cross section for doubly charged Higgs boson pairs is significantly lower than that in the $\gamma\gamma$ mode over most of the kinematically allowed mass range. However, as the primary operational mode of CLIC, $e^+e^-$ collisions accumulate a much higher integrated luminosity, enabling a $5\sigma$ discovery reach for $H^{\pm\pm}$ up to a mass of approximately 1200 GeV with an integrated luminosity of 5 ab$^{-1}$.

For comparison, we also evaluate the feasibility of probing the doubly charged Higgs boson through the pair-production channel at the HL-LHC. Our analysis shows that the HL-LHC yields a lower observation signi-

CPC Accepted

ficance, primarily because of its substantially smaller production cross section relative to that at CLIC, together with a more complex background environment. In both the Yukawa-like and gauge-like regions, the HL-LHC reaches $3\sigma$ observation significance only within a narrow mass range above the experimental exclusion limit on $m_{H^{\pm\pm}}$, highlighting the superior discovery potential of CLIC for the doubly charged Higgs boson.

## References


[1] Y. Fukuda *et al*. (Super-Kamiokande Collaboration), Phys. Rev. Lett. **81**, 1562 (1998), arXiv: hepex/9807003
[2] Q. R. Ahmad *et al*. (SNO Collaboration), Phys. Rev. Lett. **89**, 011301 (2002), arXiv: nucl-ex/0204008
[3] K. Eguchi *et al*. (KamLAND Collaboration), Phys. Rev. Lett. **90**, 021802 (2003), arXiv: hep-ex/0212021
[4] N. Aghanim *et al*. (Planck Collaboration), Astron. Astrophys. **641**, A6 (2020) [Erratum: Astron. Astrophys. **652**, C4 (2021)], arXiv: 1807.06209[astro-ph.CO]
[5] M. Aker *et al*. (KATRIN Collaboration), Science **388**, 180 (2025), arXiv: 2406.13516[nucl-ex]
[6] S. Weinberg, Phys. Rev. Lett. **43**, 1566 (1979)
[7] P. Minkowski, Phys. Lett. B **67**, 421 (1977)
[8] M. Gell-Mann, P. Ramond, and R. Slansky, Conf. Proc. C **790927**, 315 (1979), arXiv: 1306.4669[hep-th]
[9] T. Yanagida, Prog. Theor. Phys. **64**, 1103 (1980)
[10] E. Ma, Phys. Rev. Lett. **81**, 1171 (1998), arXiv: hep-ph/9805219
[11] R. N. Mohapatra and G. Senjanović, Phys. Rev. Lett. **44**, 912 (1980)
[12] M. Magg and Ch. Wetterich, Phys. Lett. B **94**, 61 (1980)
[13] J. Schechter and J. W. F. Valle, Phys. Rev. D **22**, 2227 (1980)
[14] T. P. Cheng and L. F. Li, Phys. Rev. D **22**, 2860 (1980)
[15] R. Foot, H. Lew, X. G. He *et al*., Z. Phys. C **44**, 441 (1989)
[16] J. F. Gunion, R. Vega, and J. Wudka, Phys. Rev. D **42**, 1673 (1990)
[17] T. Hambye, E. Ma, and U. Sarkar, Nucl. Phys. B **602**, 23 (2001), arXiv: hep-ph/0011192
[18] A. Arhrib, R. Benbrik, M. Chabab *et al*., Phys. Rev. D **84**, 095005 (2011), arXiv: 1105.1925[hep-ph]
[19] A. G. Akeroyd and M. Aoki, Phys. Rev. D **72**, 035011 (2005), arXiv: hep-ph/0506176
[20] Z. L. Han, R. Ding, and Y. Liao, Phys. Rev. D **91**, 093006 (2015), arXiv: 1502.05242[hep-ph]
[21] M. Mitra, S. Niyogi, and M. Spannowsky, Phys. Rev. D **95**, 035042 (2017), arXiv: 1611.09594[hep-ph]
[22] Y. Du, A. Dunbrack, M. J. Ramsey-Musolf *et al*., JHEP **01**, 101 (2019), arXiv: 1810.09450[hep-ph]
[23] T. Li, JHEP **09**, 079 (2018), arXiv: 1802.00945[hep-ph]
[24] S. Ashanujjaman and K. Ghosh, JHEP **03**, 195 (2022), arXiv: 2108.10952[hep-ph]
[25] S. Ashanujjaman and S. P. Maharathy, Phys. Rev. D **107**, 115026 (2023), arXiv: 2305.06889[hep-ph]
[26] N. Ghosh, S. K. Rai, T. Samui *et al*., Phys. Rev. D **113**, 055048 (2026), arXiv: 2506.00966[hep-ph]
[27] C. Englert, M. Mitra, W. Naskar *et al*., arXiv: 2603.09244[hep-ph]
[28] G. Apollinari, I. Béjar Alonso, O. Brüning *et al*., *High-Luminosity Large Hadron Collider (HL-LHC): Preliminary Design Report*, CERN Yellow Reports: Monographs (CERN, Geneva, 2015)
[29] A. Abada *et al*. (FCC Collaboration), Eur. Phys. J. Spec. Top. **228**, 755 (2019)
[30] B. Fuks, M. Nemevšek, and R. Ruiz, Phys. Rev. D **101**, 075022 (2020), arXiv: 1912.08975[hep-ph]
[31] P. Fileviez Pérez, T. Han, G. Huang *et al*., Phys. Rev. D **78**, 015018 (2008), arXiv: 0805.3536[hep-ph]
[32] P. S. B. Dev, S. Khan, M. Mitra *et al*., Phys. Rev. D **99**, 115015 (2019), arXiv: 1903.01431[hep-ph]
[33] S. Godfrey, P. Kalyniak, and N. Romanenko, Phys. Lett. B **545**, 361 (2002), arXiv: hepph/0207240
[34] P. Agrawal, M. Mitra, S. Niyogi *et al*., Phys. Rev. D **98**, 015024 (2018), arXiv: 1803.00677[hep-ph]
[35] S. Ashanujjaman, K. Ghosh, and K. Huitu, Phys. Rev. D **106**, 075028 (2022), arXiv: 2205.14983[hep-ph]
[36] N. Das, D. K. Ghosh, N. Ghosh *et al*., arXiv: 2602.02308[hep-ph]
[37] J. F. Gunion, Int. J. Mod. Phys. A **11**, 1551 (1996), arXiv: hep-ph/9510350
[38] S. Godfrey, P. Kalyniak, and N. Romanenko, Phys. Rev. D **65**, 033009 (2002), arXiv: hepph/0108258
[39] X. S. Su, C. X. Yue, J. Zhang *et al*., Commun. Theor. Phys. **56**, 709 (2011), arXiv: 1010.4633[hep-ph]
[40] S. Chakrabarti, D. Choudhury, R. M. Godbole *et al*., Phys. Lett. B **434**, 347 (1998), arXiv: hep-ph/9804297
[41] A. Das, S. Mandal, and S. Shil, Phys. Rev. D **108**, 015022 (2023), arXiv: 2304.06298[hep-ph]
[42] T. Li, C. Y. Yao, and M. Yuan, JHEP **03**, 137 (2023), arXiv: 2301.07274[hep-ph]
[43] S. P. Maharathy and M. Mitra, Phys. Lett. B **844**, 138105 (2023), arXiv: 2304.08732[hep-ph]
[44] J. C. Jia, Z. L. Han, F. Huang *et al*., Phys. Rev. D **111**, 015009 (2025), arXiv: 2409.16582[hep-ph]
[45] M. Aicheler, P. N. Burrows, N. Catalan *et al*., *The Compact Linear Collider (CLIC) - Project Implementation Plan*, CERN Yellow Reports: Monographs (CERN, Geneva, 2018)
[46] D. Schulte, Int. J. Mod. Phys. A **18**, 2851 (2003)
[47] E. Accomando *et al*. (CLIC Physics Working Group), *Physics at the CLIC Multi-TeV Linear Collider*, CERN Yellow Reports: Monographs (CERN, Geneva, 2004)
[48] S. Biondini and O. Panella, Phys. Rev. D **92**, 015023 (2015), arXiv: 1411.6556[hep-ph]
[49] T. Asaka, H. Ishida, and K. Tanaka, Prog. Theor. Exp. Phys. **2025**, 113B01 (2025), arXiv: 2412.08015[hep-ph]
[50] P. Dey, A. Kundu, and B. Mukhopadhyaya, J. Phys. G **36**, 025002 (2009), arXiv: 0802.2510[hep-ph]
[51] N. Haba, H. Ishida, N. Okada *et al*., Eur. Phys. J. C **76**, 333 (2016), arXiv: 1601.05217[hep-ph]
[52] P. S. B. Dev, C. M. Vila, and W. Rodejohann, Nucl. Phys. B **921**, 436 (2017), arXiv: 1703.00828[hep-ph]
[53] E. J. Chun, H. M. Lee, and P. Sharma, JHEP **11**, 106 (2012), arXiv: 1209.1303[hep-ph]
[54] C. Bonilla, R. M. Fonseca, and J. W. F. Valle, Phys. Rev. D **92**, 075028 (2015), arXiv: 1508.02323[hep-ph]
[55] R. Primulando, J. Julio, and P. Uttayarat, JHEP **08**, 024 (2019), arXiv: 1903.02493[hep-ph]


CPC Accepted

[56] S. Navas *et al*. (Particle Data Group), Phys. Rev. D **110**, 030001 (2024)
[57] M. Aaboud *et al*. (ATLAS Collaboration), Eur. Phys. J. C **78**, 199 (2018), arXiv: 1710.09748[hep-ex]
[58] G. Aad *et al*. (ATLAS Collaboration), Eur. Phys. J. C **83**, 605 (2023), arXiv: 2211.07505[hep-ex]
[59] G. Aad *et al*. (ATLAS Collaboration), JHEP **06**, 146 (2021), arXiv: 2101.11961[hep-ex]
[60] CMS Collaboration, CMS-PAS-HIG-16-036
[61] A. M. Sirunyan *et al*. (CMS Collaboration), Eur. Phys. J. C **81**, 723 (2021), arXiv: 2104.04762[hep-ex]
[62] G. Aad *et al*. (ATLAS Collaboration), Phys. Lett. B **860**, 139137 (2025), arXiv: 2407.10798[hep-ex]
[63] G. Aad *et al*. (ATLAS Collaboration), Phys. Rev. Lett. **125**, 051801 (2020), arXiv: 2002.12223[hep-ex]
[64] A. M. Sirunyan *et al*. (CMS Collaboration), JHEP **09**, 007 (2018), arXiv: 1803.06553[hep-ex]
[65] U. Bellgardt *et al*. (SINDRUM Collaboration), Nucl. Phys. B **299**, 1 (1988)
[66] B. Aubert *et al*. (BABAR Collaboration), Phys. Rev. Lett. **104**, 021802 (2010), arXiv: 0908.2381[hep-ex]
[67] Y. Amhis *et al*. (HFLAV)Collaboration), Eur. Phys. J. C **77**, 895 (2017), arXiv: 1612.07233[hep-ex]
[68] D. Hanneke, S. Fogwell, and G. Gabrielse, Phys. Rev. Lett. **100**, 120801 (2008), arXiv: 0801.1134[physics.atom-ph]
[69] G. W. Bennett *et al*. (Muon (g − 2) Collaboration), Phys. Rev. D **73**, 072003 (2006), arXiv: hep-ex/0602035
[70] L. Willmann, P. V. Schmidt, H. P. Wirtz *et al*., Phys. Rev. Lett. **82**, 49 (1999), arXiv: hepex/9807011
[71] J. Abdallah *et al*. (DELPHI Collaboration), Eur. Phys. J. C **45**, 589 (2006), arXiv: hep-ex/0512012
[72] P. S. B. Dev and Y. Zhang, JHEP **10**, 199 (2018), arXiv: 1808.00943[hep-ph]
[73] I. F. Ginzburg, G. L. Kotkin, V. G. Serbo *et al*., Nucl. Instrum. Meth. **205**, 47 (1983)
[74] F. Boudjema, Pramana **51**, 249 (1998), arXiv: hep-ph/9809220
[75] I. F. Ginzburg and G. L. Kotkin, arXiv: 1910.13961[hep-ph]
[76] A. Alloul, N. D. Christensen, C. Degrande *et al*., Comput. Phys. Commun. **185**, 2250 (2014), arXiv: 1310.1921[hep-ph]
[77] J. Alwall, R. Frederix, S. Frixione *et al*., JHEP **07**, 079 (2014), arXiv: 1405.0301[hep-ph]
[78] O. Brunner, P. N. Burrows, S. Calatroni *et al*., arXiv: 2203.09186[physics.acc-ph]
[79] P. Artoisenet, R. Frederix, O. Mattelaer *et al*., JHEP **03**, 015 (2013), arXiv: 1212.3460[hep-ph]
[80] C. Bierlich, S. Chakraborty, N. Desai *et al*., SciPost Phys. Codeb. **2022**, 8 (2022), arXiv: 2203.11601[hep-ph]
[81] J. de Favereau *et al*. (DELPHES 3 Collaboration), JHEP **02**, 057 (2014), arXiv: 1307.6346[hep-ex]
[82] E. Leogrande, P. Roloff, U. Schnoor *et al*., arXiv: 1909.12728[hep-ex]
[83] M. Cacciari, G. P. Salam, and G. Soyez, Eur. Phys. J. C **72**, 1896 (2012), arXiv: 1111.6097[hep-ph]
[84] M. Boronat, J. Fuster, I. García *et al*., Phys. Lett. B **750**, 95 (2015), arXiv: 1404.4294[hep-ex]
[85] M. Boronat, J. Fuster, I. Garcia *et al*., Eur. Phys. J. C **78**, 144 (2018), arXiv: 1607.05039[hep-ex]
[86] E. Conte, B. Fuks, and G. Serret, Comput. Phys. Commun. **184**, 222 (2013), arXiv: 1206.1599[hep-ph]

CPC Accepted